UNIVERSITÀ DEGLI STUDI DI PADOVA

Dipartimento di Fisica e Astronomia "Galileo Galilei"

Corso di Laurea in Fisica

Tesi di Laurea

Simulazioni Fluide del Plasma nella Sorgente di Ioni Negativi - SPIDER

Fluid Simulations of the Plasma in the Negative Ion Source - SPIDER

Relatore

Dr. Gianluigi Serianni

Correlatori

Prof. Roman Zagórski

Dr. Emanuele Sartori

Laureando

Federico Faustini

Anno Accademico 2021/2022

Abstract

Simulazioni Fluide del Plasma nella Sorgente di Ioni Negativi - SPIDER

Federico Faustini

Università degli Studi di Padova

Il reattore a fusione nucleare ITER sarà riscaldato da fasci di neutri veloci generati dall'accelerazione e neutralizzazione di ioni negativi, prodotti in un plasma accoppiato induttivamente in RF e che si espande in una regione contenente un filtro magnetico. In questa tesi è presentato un modello fluido bidimensionale autoconsistente della sorgente, basato su equazioni di continuità separate per le differenti specie di particelle, l'equazione di Poisson per il potenziale di plasma e l'equazione di bilancio energetico degli elettroni per la temperatura elettronica. Inoltre, i flussi di particelle sono calcolati assumendo l'approssimazione "drift-diffusion". Il metodo numerico, basato su uno schema semi-implicito, utilizza l'approssimazione di volume finito e adotta una discretizzazione a 9 punti in modo da prendere in considerazione l'anisotropia dovuta al campo magnetico. In più, il metodo numerico è implementato da un codice in FORTRAN 95 (FSFS2D) che è stato testato in fase di sviluppo l'anno scorso in una geometria semplificata rettangolare. Le simulazioni attuali tengono conto di una geometria più accurata e realistica rispetto ai reali driver di SPIDER. È investigata l'influenza del potenziale di bias, del campo magnetico, della pressione del gas neutro e della potenza a radio-frequenza sulle proprietà del plasma e si instaura un confronto con i precedenti risultati in geometria semplificata. Si mostra come la geometria più corretta di SPIDER fornisca risultati in generale accordo con quelli ottenuti nel caso rettangolare con, tuttavia, significative differenze nella regione del driver.

Fluid Simulations of the Plasma in the Negative Ion Source - SPIDER

Federico Faustini

University of Padua

The ITER fusion reactor will be heated by fast neutral beams generated by accelerating and neutralizing negative ions, produced in a RF inductively-coupled plasma and expanding through a region featuring a magnetic filter. In this thesis a self-consistent two-dimensional fluid model of the source is presented based on separate continuity equations for the different particle species, Poisson equation for the plasma potential and the electron energy balance equation for the electron temperature. In addition, the particle fluxes are calculated assuming the drift-diffusion approximation. The numerical method, based on a semi-implicit scheme, makes use of the finite volume approximation and the 9-points-discretization is exploited in order to take into account the anisotropy due to the magnetic field. Furthermore, the numerical method is implemented in a FORTRAN 95 code (FSFS2D) which was tested in the development phase on a simplified rectangular geometry during the last year. The present simulations take into consideration a more realistic and accurate geometry with respect to the real driver volumes in SPIDER. Influence of the bias potential, magnetic field, neutral gas pressure and radio-frequency power on the plasma properties is investigated and compared with the previous results in simplified geometry. It is shown that for the more correct SPIDER geometry results are generally in agreement with the ones obtained from the rectangular case with however significant differences in the driver region.

Contents

Chapter 1

Introduction

SPIDER is the prototype of a negative ion source, built at the Consorzio RFX (Padua, Italy), in which radio-frequency (RF) power is inductively coupled to the plasma [2]. The source is part of the neutral beam injection (NBI) system [1] of the international fusion experiment ITER, still under construction at the moment. As a matter of fact, the latter will be heated by fast neutral beams generated by accelerating and neutralising negative ions produced by the source. Since the negative hydrogen ions have a low binding energy, they are easily neutralised (stripping). For this purpose, the aforementioned ion-beam source works at low gas pressure to reduce stripping losses, $P \simeq 0.3\ Pa$, though still enough to produce the plasma and negative ions.
The source also features a total of 8 driver volumes and an expansion chamber (EC), where a magnetic filter (MF) is present [1, 19, 20]. The MF plays an important role in reducing the electron temperature and the quantity of co-extracted electrons, resulting in a better source functioning [4]. On the driver-opposite side of the EC, instead, the plasma grid (PG) is installed to be used as negative ion extraction surface. A small amount of caesium is needed to enhance source performances [18].
Theoretical modelling is exploited to enrich the knowledge of the behaviour of the source discharge, in a complementary way with respect to the experiments on the prototype. The two most common approaches used for the main models of ITER sources, as reported in [20], are the particle-in-cell [5] and the fluid [11] codes. Whereas the former is well-suited for a more precise description of heavy particle dynamics and thus the negative ion extraction, as downside it cannot be easily implemented in high plasma density and large volumes conditions and currently the driver region description is strongly simplified.
The fluid plasma model implemented in the 2D code FSFS2D (Fluid Solver For Spider in 2D), overviewed in this thesis as brief continuation of the work reported in [20], has the advantage that it is not constrained by high plasma density or large volumes limits, although, on the other hand, it neglects the negative ion extraction process. It provides, anyway, a clear and precise picture of the physical phenomena which determine the evolution of plasma parameters. The presented model consists in a self-consistent two-dimensional fluid description of the source based on separate continuity equations for the different particle species. It employs Poisson equation for the plasma potential and electron temperature is given by the electron energy balance. For this purpose the particle fluxes are calculated in agreement with the drift-diffusion approximation [10].
The code numerical method is based on a semi-implicit scheme and assumes the finite volume approximation. The 9-points-approximation is used to consider the anisotropy introduced by the presence of the magnetic filter field. The FSFS2D code numerical stability and efficiency was tested during the course of the development phase in a rectangular geometry [20], specifically a 51×51 mesh grid.
The simulations presented in the following aim to take into account a more correct SPIDER geometry with respect to the rectangular geometry considered in the simulations shown in [20]. Therefore, the purpose of this thesis is to investigate the effects of this new configuration, alongside their influence on the plasma parameters in the absence and in the presence of the magnetic filter.

Chapter 2

Physical model

The current model aims at representing a two-dimensional section of SPIDER, cut through one of the eight cylindrical-drivers axis, which also includes a section of the expansion chamber, to which drivers are connected. A schematic picture of the integration domain may be found in fig. 2.1 and chapt. 5, fig. 5.3. This physical description of the source considers a low pressure hydrogen discharge with magnetised plasma, which is restricted to a 2D-section plane. The model assumes that the behaviour of each plasma species is well-represented by a Maxwell-Boltzmann distribution, considering high density and highly collisional plasmas. Starting from that, continuity equations are solved for the density of each particle species considered by the model: electrons, three positive ion species [(1) H^+ , (2) H_2^+, (3) H_3^+], negative hydrogen ions (H^-) and finally atomic hydrogen (H); the density of the molecular hydrogen (H_2) is instead calculated from the state equation of the ideal gas [20, 11]. Then the electron temperature is obtained using the electron energy balance equation. The other neutral and ion species are instead assumed with uniform gas temperatures [20, 11]. The electrostatic potential is calculated from a Poisson equation, as reported in [11]. Finally, the model considers the drift-diffusion approximation to solve the equations of motion and calculate the different fluxes.

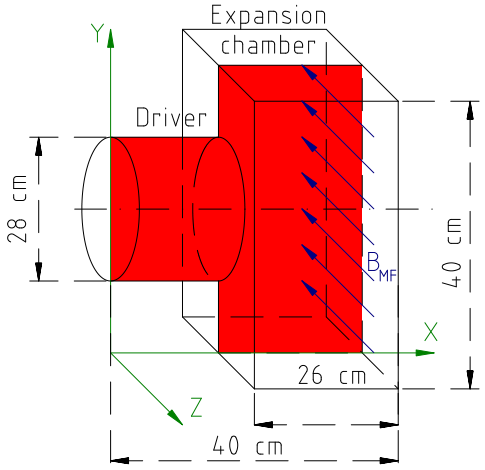

Figure 2.1: 3D representation of the source and the 2D section as integration domain [20].

2.1 Equations of continuity

Introducing the distribution functions $f(\boldsymbol{r}, \boldsymbol{w}, t)$ that characterise the behaviour of each particle species in ionised-state gas, as function of the phase-space $\Omega = (\boldsymbol{r}, \boldsymbol{w})$ and time t, where $\boldsymbol{r}$ stands for the particle position in three-dimensional space and $\boldsymbol{w}$ for the respective particle velocity, the system may be described by Maxwell-Boltzmann equations [10].

$$\frac{\partial f_a}{\partial t} + \boldsymbol{w}_a \cdot \boldsymbol{\nabla}_{\boldsymbol{r}} f_a + \frac{\boldsymbol{F}_a(\boldsymbol{r}, \boldsymbol{w})}{m_a} \cdot \boldsymbol{\nabla}_{\boldsymbol{w}} f_a = C_a = \sum_b C_{ab}(f_a, f_b) \tag{2.1}$$

C_a represent a collisional term, which in general depends on the distribution functions of the different particle species. Integrating with respect to the particle velocity $\boldsymbol{w}$, the continuity equation is found for each of the N particle species.

$$\frac{\partial n_a}{\partial t} + \boldsymbol{\nabla_r} \cdot (n_a \boldsymbol{v}_a) = S_a = Z_a - L_a \qquad \forall\ a = 1, \dots, N\ , \tag{2.2}$$

where density $n_a(\boldsymbol{r}, t) = \int f_a(\boldsymbol{r}, \boldsymbol{w}, t) d^3w$, mean velocity $\boldsymbol{v}_a(\boldsymbol{r}, t) = \langle \boldsymbol{w} \rangle_a = \frac{1}{n_a} \int \boldsymbol{w} f_a(\boldsymbol{r}, \boldsymbol{w}, t) d^3w$ and particle flux $\boldsymbol{\Gamma}_a = n_a \boldsymbol{v}_a$ are defined. Finally, S_a indicates the net number of particles of that species created per unit of volume and time. Z_a and L_a distinguish respectively between creation and destruction of particles.

The collisional term in (2.1) is zero when integrated over velocity, but not for collisions creating or destroying particles of the given species. For low pressure gas, Z_a is mainly associated with electron ionisation whereas L_a with recombination, which is often negligible. S_a assumes the general form of $S_a = \sum_b N_b n_{i_b} n_{j_b} k_b$, with n_{i_b} and n_{j_b} the colliding particle species density, N_b the number of particles produced in the event and k_b a rate coefficient [11]. The model fallows the more detailed plasma kinetic description given by J. Santoso [16].

n°	Reaction	React. type
1	$e + H_2 \rightarrow H_2^+ + 2e$	Ionis.
2	$e + H_2 \rightarrow 2H + e$	Diss.
3	$e + H_2 \rightarrow H + H^-$	Diss. att.
4	$e + H \rightarrow H^+ + 2e$	Ionis.
5	$H + H_2^+ \rightarrow H_2 + H^+$	Char. exch.
6	$e + H_2^+ \rightarrow H + H^+ + e$	Diss.
7	$e + H_3^+ \rightarrow H_2^+ + H^-$	Ion-pair pr.
8	$H_2 + H_2^+ \rightarrow H + H_3^+$	Part. exch.
9	$H^+ + H^- \rightarrow 2H$	Mut. nuet.
10	$H_2^+ + H^- \rightarrow H_2$	Mut. nuet.
11	$H_3^+ + H^- \rightarrow \frac{1}{2}H_2 + 3H$	Mut. nuet.
12	$e + H^- \rightarrow H + 2e$	Elec. att.
13	$e + H_3^+ \rightarrow 2H + H^+ + e$	Diss.
14	$H_2 + H^+ \rightarrow H_3^+ + h\nu$	Rad. ass.
15	$e + H_2^+ \rightarrow 2H$	Diss. rec.
16	$e + H_3^+ \rightarrow 3H$	Diss. rec.
17	$e + H_3^+ \rightarrow H + H_2$	Diss. rec.
18	$H + H^- \rightarrow H_2 + e$	Neut. det.
19	$H_2 + H^- \rightarrow H + H_2 + e$	Neut. det.
20	$H + H^- \rightarrow 2H + e$	Neut. det.
21	$H_2 + H^+ \rightarrow H + H_2^+$	Char. exch.
22	$e + H \rightarrow H^- + h\nu$	Rad. att.

Table 2.1: Reactions accounted by the model.

As a matter of fact, hydrogen admits 6 ground-state forms: molecular and atomic hydrogen, three positive and one negative ions. There are also many electronically and vibrationally excited, meta-stable and transitional states which may contribute to the plasma chemistry of the system, but they are not considered in the model. All the reactions contributing to the particle balances are listed in the table 2.1 following [20]. These include ionisation and dissociation of molecules, dissociation of H_2^+ and H_3^+ ions, dissociative recombination of H_2^+ ions, heavy particle collisions, ionisation of atoms and H^- destruction. Due to the difficulty of solving H_2 continuity equation, which would entail precise knowledge of SPIDER pumping system and geometry, n_{H_2} is directly obtained from the state equation of the ideal gas, with the assumption of uniform neutrals temperature [20].

2.2 Equation of motion & drift-diffusion approximation

Multiplying (2.1) by $m_a \boldsymbol{w}$ and integrating over velocity, the momentum conservation equation is obtained for each vector component.

$$\frac{\partial (m_a n_a v_{a,i})}{\partial t} + \sum_{j=1}^{3} \frac{\partial (m \langle n_a w_{a,i} w_{a,j} \rangle)}{\partial x_j} - n_a F_{a,i} = \int m_a w_{a,i}\, C_a d^3w \quad \forall\, i = 1, 2, 3 \tag{2.3}$$

Then, the velocity $\boldsymbol{u}_a = \boldsymbol{w} - \boldsymbol{v}_a$ is defined. Since the integration is over velocity and n_a is not affected and mixed-velocity term may be rearranged in $\langle w_{a,i} w_{a,j} \rangle = v_{a,i} v_{a,j} + \langle u_{a,i} u_{a,j} \rangle$. The pressure tensor is defined as $P_{ij}^{(a)} = n_a m_a \langle u_i u_j \rangle$ and, after few manipulation, the equation (2.3) can be reformulated as follows [10, 7, 3].

$$m_a \frac{\partial n_a \boldsymbol{v}_a}{\partial t} + m \boldsymbol{v}_a (\boldsymbol{\nabla_r} \cdot (n_a \boldsymbol{v}_a)) + m_a n_a (\boldsymbol{v}_a \cdot \boldsymbol{\nabla_r}) \boldsymbol{v}_a + \boldsymbol{\nabla_r} \cdot \hat{\boldsymbol{P}}_a - n_a \boldsymbol{F}_a = \boldsymbol{R}_a = \int m_a \boldsymbol{u}_a C_a d^3w \tag{2.4}$$

In this case, $\boldsymbol{R}_a$ stands for the change of momentum of the particle of a given species due to collisions with other particle species.
Using (2.2) in (2.4), the equation of motion ($a = 1, \dots, N$) is obtained [3].

$$m_a n_a \frac{\partial \boldsymbol{v}_a}{\partial t} + m_a n_a (\boldsymbol{v}_a \cdot \boldsymbol{\nabla}_{\boldsymbol{r}}) \boldsymbol{v}_a + \boldsymbol{\nabla}_{\boldsymbol{r}} \cdot \hat{\boldsymbol{P}}_a = n_a \boldsymbol{F}_a + \boldsymbol{R}_a - m_a S_a \boldsymbol{v}_a \tag{2.5}$$

The force $\boldsymbol{F}_a$, in addition to the usual contribution from the Lorentz force, may also contain other effects related e.g. to RF heating [7], which are labelled in the following as "$\boldsymbol{F}_{add}$". Furthermore, $\boldsymbol{R}_a$ indicates the rate of momentum transfer per unit volume due to both elastic and non-elastic collisions. It also can be written as a function of the difference between the mean velocities of the a-species particles and of the other particle species [3]. Since in weakly ionised plasma collisions with neutrals are dominant ($\boldsymbol{v}_{neut} = 0$) and the mean velocity of the newly created or destructed particles in pair creation due to ionisation is negligible compared to $\boldsymbol{v}_a$, it is assumed that $\boldsymbol{R}_a$ only depends on $\boldsymbol{v}_a$ and not on the differences with the mean velocity of the other particle species, as a first approximation. Finally, supposing that the pressure tensor is diagonal (scalar pressure P_a), the equation of motion can be rewritten in the following form [7].

$$m_a n_a \frac{\partial \boldsymbol{v}_a}{\partial t} + m_a n_a (\boldsymbol{v}_a \cdot \boldsymbol{\nabla}_{\boldsymbol{r}}) \boldsymbol{v}_a + m_a n_a \widetilde{\nu}_a \boldsymbol{v}_a = n_a \boldsymbol{F}_a - \boldsymbol{\nabla}_{\boldsymbol{r}} P_a \ , \tag{2.6}$$

where the overall collision frequency, which considers the particle generation processes, is written as $\widetilde{\nu}_a = \sum_j \frac{m_j}{m_a + m_j} n_j \nu_{aj} + \frac{S_a}{n_a}$, with the collision frequency ν_{aj} between species a and j. From the scalar pressure, the temperature of each particle species is also defined: $P_a = n_a \, e \, T_a$, with e being the elementary charge. The gas pressure is then defined by the neutral species as $P_g = e \, T_g \, (n_H + n_{H_2})$ [11]. Note that, unless explicitly stated, all temperatures are expressed in volts (V).

Drift-diffusion approximation. As main assumption of the model, it is supposed that the inertial terms in (2.6) can be neglected due to their modest contribution in comparison with collisions [20]. Therefore, according to the shortness of the diffusive time scale, acceleration $\frac{\partial \boldsymbol{v}_a}{\partial t}$ and inertial term $(\boldsymbol{v}_a \cdot \boldsymbol{\nabla}_{\boldsymbol{r}}) \boldsymbol{v}_a$ are considered negligible and (2.6) can provide an expression for the flux.

$$\boldsymbol{\Gamma}_a = n_a \boldsymbol{v}_a = \frac{n_a}{m_a \widetilde{\nu}_a} \boldsymbol{F}_a - \frac{1}{m_a \widetilde{\nu}_a} \boldsymbol{\nabla}_{\boldsymbol{r}} P_a \tag{2.7}$$

This can be rearranged as reported, e.g. for electrons, in [7]; the particle species subscript a will be omitted for simplicity as well as subscript $\boldsymbol{r}$ for $\boldsymbol{\nabla}$ operator. The last convention will be followed from this point onwards. The following equation, as illustrated in [7], offers also a definition for the mobility tensor $\hat{\boldsymbol{\mu}}$.

$$\boldsymbol{\Gamma} \equiv \frac{\hat{\boldsymbol{\mu}}}{\mu} \boldsymbol{G} = \frac{(\boldsymbol{G} + \mu \boldsymbol{B} \times \boldsymbol{G} + \mu^2 (\boldsymbol{B} \cdot \boldsymbol{G}) \boldsymbol{B})}{1 + (\mu B)^2} \ , \tag{2.8}$$

with $\boldsymbol{G}$ and μ, which are respectively the drift-diffusion flux and the scalar mobility coefficient without the magnetic field and defined as fallows for $\boldsymbol{F} = q(\boldsymbol{E} + \boldsymbol{v} \times \boldsymbol{B}) + \boldsymbol{F}_{add}$, which also accounts for the additional contribution term $\boldsymbol{F}_{add}$ due to the RF-heating.

$$\boldsymbol{G} = n \mu \frac{q}{|q|} \boldsymbol{E} - \frac{neD}{|q|} \left(\frac{\boldsymbol{\nabla} n}{n} + \frac{\boldsymbol{\nabla} T}{T} \right) + n \frac{\mu}{|q|} \boldsymbol{F}_{add} \ , \tag{2.9}$$

where $D \equiv \mu T$ for Einstein's equation and $\mu = \dfrac{|q|}{m \widetilde{\nu}}$, with q being the particle charge.

For the neutral species, fluxes are instead calculated as diffusion fluxes, according to their uniform temperature [11]: $\boldsymbol{\Gamma}_a = -D_a \boldsymbol{\nabla} n_a$, where D_a is the (scalar) diffusion coefficient.
Assuming the magnetic filter field to have the form described in [11] ($\boldsymbol{B} = (0, 0, B_z)$ is perpendicular to the integration domain plane $z = 0$), the mobility tensor takes the following form with anisotropic off-diagonal components.

$$\hat{\boldsymbol{\mu}} = \begin{pmatrix} \frac{\mu}{1+\mu^2 B_z^2} & \frac{q}{|q|} \frac{\mu^2 B_z}{1+\mu^2 B_z^2} & 0 \\ -\frac{q}{|q|} \frac{\mu^2 B_z}{1+\mu^2 B_z^2} & \frac{\mu}{1+\mu^2 B_z^2} & 0 \\ 0 & 0 & \mu \end{pmatrix} \tag{2.10}$$

Therefore, when there is no magnetic field μ becomes just a multiple of the identity tensor. However, in the presence of the field, inside the expansion chamber the mobility perpendicular to $\boldsymbol{B}$ is considerably reduced due to the fact that the so-called Hall term (adimensional), μB_z, assumes remarkably high values, even greater than 100 in the case, for instance, of electrons. That implicates a severe reduction in perpendicular transport [7]. In particular, it also affects the electron thermal conductivity with a strong decrease, given that the latter is defined as $\hat{\boldsymbol{\chi}}_e = \frac{5}{2}\hat{\boldsymbol{D}}_e = \frac{5}{2}\hat{\boldsymbol{\mu}}_e T_e$ [20].

2.3 Energy balance and Poisson equation

Assuming the force in (2.1) to be of the form $\boldsymbol{F} = q(\boldsymbol{E} + \boldsymbol{v} \times \boldsymbol{B})$, multiplying the Maxwell-Boltzmann equation by $\frac{1}{2}m_a w^2$ and integrating over velocity, after a few manipulation and supposing that the *pressure tensor is diagonal*, the energy conservation equation is expressed according to [3].

$$\begin{aligned} \frac{\partial}{\partial t}\left(\frac{m_a n_a}{2}v_a^2 + \frac{3}{2}n_a e T_a\right) + \sum_{i=1}^{3}\frac{\partial}{\partial r_i}\left[\left(\frac{m_a n_a}{2}v_a^2 + \frac{5}{2}n_a e T_a\right)v_{a,i}\right] + \\ + \boldsymbol{\nabla}\cdot\boldsymbol{h}_a = q_a n_a \boldsymbol{E}\cdot\boldsymbol{v}_a + \boldsymbol{R}_a\cdot\boldsymbol{v}_a + Q_a \ , \end{aligned} \tag{2.11}$$

with the flux density of heat $\boldsymbol{h}_a = n_a m_a \langle \frac{u_a^2}{2}\boldsymbol{w}\rangle$ and $Q_a = \int \frac{m_a u_a^2}{2} C_a d^3 w$ as collisional power generated by collisions between particles of different species.

For this purpose, it is possible to define a temperature even though the gas is not in thermal equilibrium, in a coordinate system such that $\boldsymbol{v}_a = 0$: $P_a = n_a e T_a(\boldsymbol{r}, t) = \frac{m_a}{3}\langle(\boldsymbol{w} - \boldsymbol{v}_a)^2\rangle$ [3].

Limiting the equation to electrons and assuming that for collisional particles the heat flux takes the form $\boldsymbol{h}_e = -e\, n_e \frac{5}{2}\hat{\boldsymbol{D}}_e \boldsymbol{\nabla} T_e$ (for unmagnetised particles the diffusion tensor $\hat{\boldsymbol{D}}_e = \hat{\boldsymbol{\mu}}_e T_e$ shall be replaced by the scalar diffusion coefficient $D_e = \mu_e T_e$), the expression for the electron energy balance equation is derived as reported in [7], in which the $\frac{1}{2}m_e v_e^2$ directed kinetic energy term is negligible with respect to the other ones due to small value of m_e.

$$\frac{3}{2}\frac{\partial n_e T_e}{\partial t} + \frac{5}{2}\boldsymbol{\nabla}\cdot(n_e T_e \boldsymbol{v}_e - n_e \hat{\boldsymbol{D}}_e \boldsymbol{\nabla} T_e) = n_e \boldsymbol{E}\cdot\boldsymbol{v}_e + \frac{1}{e}Q_e + \frac{1}{e}P_{RF} \tag{2.12}$$

For the electron energy balance equation, the additional term P_{RF} represents the RF-power deposition averaged over a RF-cycle as explained in [20].
The collisional power term $Q_e = -P_e^{coll}$ is usually negative and it consists of two parts which take into account respectively the different inelastic collision processes such as excitation and ionisation and the elastic energy transfer [7]. The main processes that lead to energy loss considered by the model are ionisation of atomic or molecular hydrogen, dissociation of hydrogen molecules, dissociative attachment, ion-pair production, excitation of H and H_2 and elastic collisions of atoms and molecules (all included in P_e^{coll}) [11], see tab. 2.1.
From this equation, T_e can be computed, whereas the temperatures of the other particles species are assumed uniform and constant as mentioned. In particular, the gas temperature $T_g = 700\,K$ and the ion temperature $T_i = 1000\,K$ are taken in all presented further simulations.

Poisson equation for the potential. Finally, the equation to determine self-consistently the electric field is the Poisson equation which is presented in [20, 11, 7].

$$\nabla^2\Phi = -\frac{e}{\epsilon_0}\left(\sum_{i=1}^{3} n_i - n_e - n_{H^-}\right) \ , \tag{2.13}$$

with the $i = 1, 2, 3$ index standing for the three different positive hydrogen ions. $\boldsymbol{E} = -\boldsymbol{\nabla}\Phi$ is the dc electric field generated by the spatial gradient of the plasma potential and ϵ_0 the vacuum permittivity [20].

2.4 Boundary conditions

These fluid equations are solved in a spatial domain which includes closed boundaries, i.e. the physical walls. For this reason it is necessary to appropriately formulate a set of wall-flux boundary conditions to take into account the physical processes occurring when particles come to and interact with the walls. In this model the same prescription given in [20, 11] has been followed, distinguishing particles coming and going away from the walls with a net perpendicular flux to the walls: $nv_\perp = \hat{\boldsymbol{e}}_{wall} \cdot \boldsymbol{\Gamma} = nv_{wall} - \Gamma_{wall}$. Both v_{wall} and Γ_{wall} are positive by definition and indicate respectively the effective wall loss speed of particles towards the wall and the flux of particle reflected or created at the wall and coming into the plasma. Regarding the potential, the boundary conditions set conventionally the potential of the metallic walls to zero, with respected to which the plasma grid positive bias potential is also given [11, 20]. In particular, the negative ion extraction at the plasma grid is beyond the purpose of this model, thus the boundary conditions for H^- ions at the PG is simplified [11]. The expression for the H^- flux perpendicular to the plasma grid is made of a flux term towards the PG and another one accounting for the accumulation of ions. On the other hand, for the other metallic walls, since no negative hydrogen ions are generated, the H^- flux is assumed to be zero [11].
The general form of the flux coming from one of the walls is given by $\Gamma_w = pnv_w + \sum_k \gamma_k n_k v_{w,k}$, where p stands for the reflection probability and γ_k for the probability of creation as consequence of collision between particles of the species k [7] (γ plays a rather important role for H^-, considering the negative ions creation at the plasma grid, $\gamma_{H^-} \equiv Y$). The model implements the same boundary conditions and prescriptions given in papers [11, 8, 7] and here they are briefly summarised.
The boundary condition of the potential:

$$\Phi|_{boundary} = \begin{cases} 0 & wall \\ \Phi_{PG} & PG \end{cases} . \tag{2.14}$$

Introducing the thermal velocity of the species a as $v_{th,a} = \sqrt{\frac{8eT_a|_V}{\pi m_a}}$, the orthogonal versor to the boundary surface $\hat{\boldsymbol{e}}_b$ and indicating the 3 positive hydrogen ions by the index $j = 1, 2, 3$, the conditions to be imposed for the fluxes are:

$$\hat{\boldsymbol{e}}_b \cdot \boldsymbol{\Gamma}_e = \frac{1}{4} v_e^{(th)} n_e \ , \tag{2.15}$$

$$\hat{\boldsymbol{e}}_b \cdot \boldsymbol{\Gamma}_{H^-} = \begin{cases} 0 & wall \\ -\frac{1}{4} Y v_a^{(th)} n_a + \frac{1}{4} v_{H^-}^{(th)} n_{H^-} & PG \end{cases} , \tag{2.16}$$

$$\hat{\boldsymbol{e}}_b \cdot \boldsymbol{\Gamma}_j = \begin{cases} n_j (\hat{\boldsymbol{\mu}}_j \cdot \boldsymbol{E}) \cdot \hat{\boldsymbol{e}}_b + \frac{1}{2} v_j^{(th)} n_j \, , & (\hat{\boldsymbol{e}}_b \cdot \boldsymbol{E}) > 0 \\ \frac{1}{4} v_j^{(th)} n_j \, , & (\hat{\boldsymbol{e}}_b \cdot \boldsymbol{E}) \leqslant 0 \end{cases} , \tag{2.17}$$

$$\hat{\boldsymbol{e}}_b \cdot \boldsymbol{\Gamma}_a = \begin{cases} \frac{1}{4} \gamma v_a^{(th)} n_a & wall \\ \frac{1}{4} (\gamma + Y) v_j^{(th)} n_j & PG \end{cases} . \tag{2.18}$$

Defining $\boldsymbol{h}_e$ as the electron energy flux , the boundary condition for equation (2.12) is the following.

$$\hat{\boldsymbol{e}}_b \cdot \boldsymbol{h}_e = \frac{5}{2} e T_e (\hat{\boldsymbol{e}}_b \cdot \boldsymbol{\Gamma}_e) \tag{2.19}$$

Chapter 3

Numerical method

The fluid equations presented above are solved numerically by the FORTRAN 95 FSFS2D code. In order to take into account the time evolution of the physical quantities described by these equations throughout the two-dimentional domain, the derivatives in the equations are approximated by the finite difference method, which requires all the quantities to be evaluated in a discrete set of positions in space and points in time [20].

3.1 Time integration of the fluid equations

The purpose of the code is finding the numerical solution of the system of generalised convection-diffusion equations presented in the previous chapter. Each of those equations assumes the form that can be expressed as follows.

$$\rho\frac{\partial f}{\partial t} + \boldsymbol{\nabla}\cdot\boldsymbol{\Gamma} \equiv \rho\frac{\partial f}{\partial t} + \boldsymbol{\nabla}\cdot(\boldsymbol{w}f - \hat{\boldsymbol{D}}\cdot\boldsymbol{\nabla}f) = S \tag{3.1}$$

with f as the unknown plasma parameter function, ρ as a scalar function which becomes $\rho = 1$ for the continuity equations, $\rho = \frac{3}{2}en_e$ for the electron energy balance equation and $\rho = 0$ for Poisson equation.

In those fluid equations transport coefficients and sources couple with each other resulting in strong non-linearity and therefore a proper time discretisation must be implemented.
In the following the upper index k shall refer to the t_k point in time at which quantities are known and explicitly calculated, whereas the implicit evaluation of the unknown quantities at the next time step, $t_{k+1} = t_k + \Delta t$, will be indicated with $k+1$ [9]. The discrete position on the grid at which functions will be computed is shown as p lower index in the following discretisation of equation (3.1). The upper indices k_ρ, $k_{\boldsymbol{w}}$, k_f, $k_{\boldsymbol{D}}$ and k_S are relative to the respective quantity and may assume the value of k (explicit) or $k+1$ (implicit).

$$\frac{\rho_p^{k_\rho} f_p^{k+1} - \rho_p^k f_p^k}{\Delta t} + \boldsymbol{\nabla}\cdot(\boldsymbol{w}^{k_{\boldsymbol{w}}} f^{k_f} - \hat{\boldsymbol{D}}^{k_{\boldsymbol{D}}}\cdot\boldsymbol{\nabla}f^{k_f})|_p = S_p^{k_S} \tag{3.2}$$

where the transport and source terms can be evaluated either explicitly at t^k or implicitly at t^{k+1}. The first approach might be simpler to implement but can cause numerical fluctuations or instabilities for large time steps. On the contrary, the implicit one does not give rise to those instabilities but it is usually hard to achieve. The current code treats the function f in the transport term always following the implicit approach because otherwise the restrictive "Courant-Friedrichs-Lewy" condition [12] should be applied to the time step in order to guarantee convergence of the finite differences method, as reported in [9]. This is due to the coupling of the equations and for this reason semi-implicit schemes are often implemented to avoid it. However, for transport coefficients and sources

the explicit one is preferred because of the difficulty of handling implicitly the particle densities in the source term. In the transport term, the electric field explicit treatment involves a very severe time step condition with high plasma density, as formalised in [9]. It is also shown in [9, 7] that a semi-implicit method, instead of a fully implicit one, can be used to accomplish convergency and stability for relatively large time steps.
Finally, an iteration loop is used at each time step to ensure the convergence of the solution of this system of equations that might be highly non-linear due to the equations coupling. Here the upper index i indicates the iteration counter.

$$\frac{\rho_p^{i+1,k_\rho} f_p^{i+1,k+1} - \rho_p^k f_p^k}{\Delta t} + \boldsymbol{\nabla} \cdot (\boldsymbol{w}^{i,k_{\boldsymbol{w}}} f^{i+1,k_f} - \hat{\boldsymbol{D}}^{i,k_{\boldsymbol{D}}} \cdot \boldsymbol{\nabla} f^{i+1,k_f})|_p = S_p^{i,k_S} \tag{3.3}$$

3.2 Discretisation of generalised convection-diffusion equation

The code performs the computational calculations on a two-dimensional Cartesian non-uniform grid, consisting of a fixed number of points in each direction, on which the finite difference method is exploited. For the divergence operator the control volume method [13] is used. The method involves the so-called control volumes defined around each grid point and whose corners lie in the middle of the other points of the grid. Equation (3.1) is therefore integrated over this control volume exploiting Gauss's theorem and the resulting volume and surface integrals are approximated by simple quadratures. Then, the discretisation imposes the conservation of the flux on the above-mentioned Cartesian grid and a linear system of equations is obtained from the initial discretised differential equations. In this case the lower indices represent x and y coordinates of the mesh at which quantities are evaluated, following the convention that $x_{i+1} = x_i + \Delta x$ and $y_{j+1} = y_j + \Delta y$. For each point of the grid (x_i, y_j) the following linear equation is obtained.

$$\begin{aligned} A_{ij}^1 f_{i,j+1} + A_{ij}^2 f_{i+1,j+1} + A_{ij}^3 f_{i+1,j} + A_{ij}^4 f_{i+1,j-1} + \\ A_{ij}^5 f_{i,j-1} + A_{ij}^6 f_{i-1,j-1} + A_{ij}^7 f_{i-1,j} + A_{ij}^8 f_{i-1,j+1} + A_{ij}^9 f_{i,j} = R_{ij} \ , \end{aligned} \tag{3.4}$$

where $A_{ij}^1, \ldots, A_{ij}^9$, R_{ij} are coefficients. This way the value of f at each point of the mesh is associated to the other 8 neighbouring points (9-points method). By imposing $A_{ij}^2 = A_{ij}^4 = A_{ij}^6 = A_{ij}^8 = 0$ also the 5-points method approximation is derived as a particular case of the 9-points scheme, although only in the absence of drifts, when the diffusion tensor is isotropic, it is applicable (see section 5.1.3). As a matter of fact, only the 9-points scheme is exploitable with the magnetic field, although it might present some numerical issues resulting in point-to-point fluctuations using "SPIDER-geometry" meshes [20] as the one presented in chapter 5.

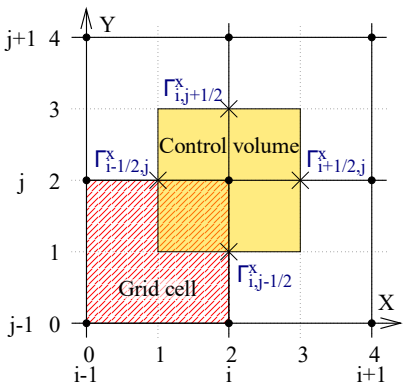

Figure 3.1: Numerical cell.

Drift-diffusion fluxes are instead discretised following the Patankar scheme [13] and evaluated at the sides of each control volume as in fig. 3.1. To guarantee the stability of the method the discretisation is made on a staggered mesh in which the vectorial quantities are evaluated in points that are half-shifted in both directions with respect to the grid points.
Finally, the scheme presented in [6] and based on the 9-points method is used to address some numerical issues regarding the anisotropy of the electron transport in the presence of a curved magnetic field.

Modified Poisson equation. The Poisson equation results to be highly coupled with charged particle equations and it would be subjected to severe time step constraints that can be avoided including into the equation a semi-implicit prediction of the space charge density [20, 7]. This way, the plasma sheath emerging from the simulations stretches out from the walls towards the plasma for a few grid cells (its width is lower-bounded by grid spacing), whose length can be many times the real thickness of the physical sheath taking into account the physical condition of the system under consideration. However, this method gives a self-consistent description of the plasma potential of the system up to the sheath, which is the important point [7]. In this model the equation is further modified considering the time derivative of potential, which is an "artificial" term that stabilises the solution-finding process.

$$\begin{aligned} &\frac{\Phi^{k+1}-\Phi^{k}}{\beta\Delta t} - \epsilon_0 \boldsymbol{\nabla}\cdot((\hat{\mathbf{1}}+\hat{\boldsymbol{\chi}})\cdot\boldsymbol{\nabla}\Phi^{k+1}) = \\ &= -e(2n_e^k - n_e^{k-1}) + \sum_i q_i(2n_i^k - n_i^{k-1}) - \epsilon_0\boldsymbol{\nabla}\cdot(\hat{\boldsymbol{\chi}}\cdot\boldsymbol{\nabla}\Phi^k)\,, \quad \text{with} \quad \beta \gg 1 \end{aligned} \tag{3.5}$$

3.3 Methods for linear systems

The finite volume discretisation of the partial differential equations introduced before leads to a large number of linear equations to be solved and therefore the overall efficiency of the program is greatly affected by the efficiency of the particular method used to solve those linear equations, which have the form: $\boldsymbol{Ax} = \boldsymbol{b}$, where $\boldsymbol{A}$ and $\boldsymbol{b}$ are respectively a matrix and a vector of coefficients. However, for the cases treated by the model, the coefficient matrix has usually a structure in which non-zero values are in only five or nine diagonals depending on the method used and therefore much memory and resources are saved. The principal methods used to solve these linear systems are the direct ones, which execute a predetermined number of steps, and the iterative ones, that aim at interactively approximating the solution better and better in a non-predetermined number of operations. Iterative methods are the most efficient for sets of a large number of equations as in the case presented. Among the direct approaches, it must be mentioned, for instance, the Gaussian elimination method.
On the other hand, regarding the iterative methods, the code implements three of them: the GMRES (General Minimalised Residual) and BiCGSTAB (Bi-Conjugate Gradient Stabilised) solvers, and incomplete factorisation scheme with the MSI (Modified Strongly Implicit) procedure [9].

3.4 Validation of the numerical approach

As illustrated in [20], using the presented method for the Poisson equation, time steps up to 1000 times larger than the characteristic time of the system can be used to obtain convergent steady-state solutions in a reasonable computational time. Furthermore, the physical model and the numerical approach implemented in the code have been tested on some simplified problems to examine overall convergence, for instance, in highly anisotropic conditions (presence of a magnetic field). It is shown that if the field lines are set to cross the integration domain border, efficient and fast convergence may be obtained. Also, plasma neutrality outside the plasma sheath emerged from simulations conducted in these simplified test cases. The same paper indicates how the corners of the two lateral vacuum zones alongside the driver can cause some local numerical issues when a SPIDER-like geometry is used instead of a rectangular one. Finally, it has been found out that in the presence of the magnetic field and the correspondent drifts, some irregularities in plasma parameters near the boundaries and difficulties in convergence arose. For this matter, mobility coefficients have been artificially altered, increasing the values of the diagonal elements with respect to the off-diagonal ones in some circumstances [20] (see paragraph 5.1.3).

Chapter 4

Description of the FSFS2D code

The **FSFS2D** (**F**luid **S**olver **F**or **S**pider in **2D**) code is written in FORTRAN 95 and is composed of 9 source files and 10 modules. A brief list of the source files is presented below, see tab. 4.1 and 4.2. The same code is used in [20].

Some input files must be defined by the user in order to run the code. `HTABLE_1D.DAT` is the first input file and contains tables necessary to calculate the rate coefficients used in the code.

The code run is controlled by a certain number of input parameters which are read from the file `InputPar.dat`.

The results are written to the file `Outputfile.dat`. This file has then to be renamed to `Inputfile.dat` when a run is started from an already saved result.

The results of simulations in a formatted form are finally written to the file `Results.dat`. This is the main output file and it is complemented by some smaller output files with profiles of some parameters .

n°	File name	Contents
1	`fsfs_v1.f90`	progr. fluidsolver-2d
2	`Arrays.f90`	module arrays
3	//	module inputpar
4	//	module inputdata
5	`Constants.f90`	module constants
6	`Physics.f90`	module physics
7	`RF_heat.f90`	module rf-heat
8	`MatrixVector.f90`	module matrix vector
9	`Numerics.f90`	module numerics
10	`Sparse9.f90`	module sparse9
11	`utilities.f90`	module utilities

Table 4.1: Contents of the files.

n°	Description
1	Main workflow, contains solver loop.
2	Dentition of main variables and its dimensions.
3	Reads input parameters.
4	Reads input data, initialisation of the program.
5	Definition of some constants used in other modules.
6	Definition of transport coefficients, sources, velocities, etc...
7	Calculates the RF field.
8	Sparse implementation of matrix-by-vector products.
9	Collection of linear iterative solvers and some preconditioners.
10	Contains routines for storage and manipulation of large sparse matrices.
11	Some useful routines which are solution independent.

Table 4.2: Description of contents of the files.

Chapter 5

Simulation results

The aim of the following analysis is to test the FSFS2D code in a more correct SPIDER geometry with respect to the rectangular one used in [20] and to understand how this change can influence the plasma parameters alongside the MF topology, the gas pressure, the plasma potential applied to the PG and the RF heating power. Therefore, for this purpose a 51×51 points mesh is introduced, which is addressed as "mesh 2", in place of the mesh used for the previous simulations in rectangular geometry, which will be called "mesh 1".

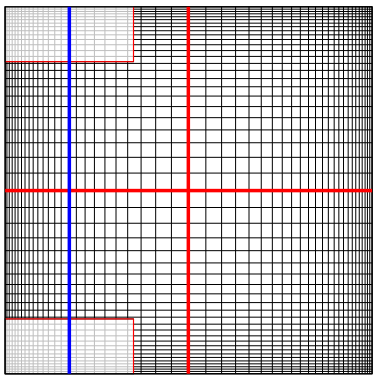

Figure 5.1: Representation of **mesh 1**. The two lateral driver regions are shown in white for comparison with mesh 2 but the points inside them were included in the integration domain.

The two meshes have the same number of points in each direction but the lateral regions of the driver are to be considered excluded from the mesh 2, since they are besides the driver walls in SPIDER geometry. The non-homogeneous distributions of points of the two meshes are different from each other in both directions: mesh 1 is symmetric with respect to the integration domain centre with closer steps near the walls ($h_i/h_{i+1} = 1.1$ [20]), whereas the more complicated mesh 2 distribution of points aims at reflecting and adapting to the more correct SPIDER geometry, as it is displayed in fig. 5.1 and fig. 5.2, respectively (more details on the grid construction are given in section 5.1.3). In both cases, the model assumes a RF heating source applied only in the whole driver region ($x \in [0\,cm,\ 14\,cm]$, $y \in [-14\,cm,\ 14\,cm]$). The power delivered to the plasma is proportional to electron density ($P_{RF} = n_e \cdot \epsilon_{RF}$, where the energy gain per electron ϵ_{RF} is a constant).

Phenomena such as the self-consistent coupling of the RF coil with the driver plasma and the local plasma conductivity are neglected, at least at the current stage of development. Regardless of specific mesh, in this model the PG is considered as a solid surface which is positively biased with respect to the source walls and put in contact with plasma (see figure 5.3). Concerning the charged particle species, the ions are treated as unmagnetised, whereas the electrons might be instead strongly magnetised. This is due to the fact that the ratio between the ion cyclotron frequency and the respective collision frequency [14] is lower than one in most of the source at the typical discharge conditions under which the simulations have been conducted. As a matter of fact, this model of hydrogen discharge at low pressure operates at the typical SPIDER test-bed operational

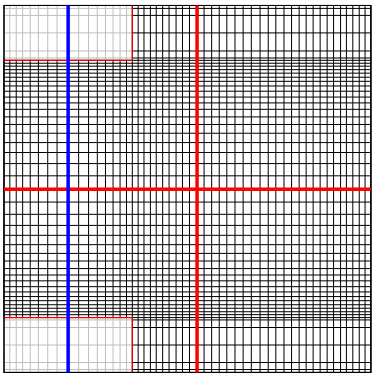

Figure 5.2: Representation of **mesh 2**. The lateral regions in this case are excluded from the simulations.

conditions: for reference, $\sim 0.3\ Pa$ of pressure, a power of $50\,kW$ and a MF field strength up to $3\,mT$ [17].
Finally, it must be specified that, although the energy balance of neutrals and positive ions might be an important matter, it is not currently considered in the model following the recommendation from [11].

5.1 Simulation results in "mesh 2" - SPIDER geometry

5.1.1 Results without magnetic field

First simulations without magnetic field were performed. In order to investigate the response of the plasma to the main discharge parameters, input parameters have been individually scanned starting from the **reference case**: **RF heating power P_{RF}=30 kW/m, PG potential Φ_{PG}=5 V and constant and uniform gas pressure P$\equiv P_g$=0.3 Pa**.

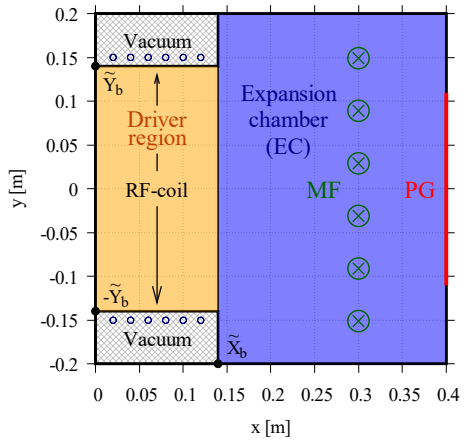

Figure 5.3: Schematic 2-D representation of the integration domain of the negative ion source as in SPIDER. The plasma grid (PG) and the magnetic filter (MF) perpendicular to the integration domain are also marked. **Mesh 2** excluded regions have $\widetilde{y}_b = \widetilde{x}_b = 0.14\ m$.

Overall behaviour, $|B|$= 0 mT. The following 2-dimensional plots in fig. 5.4 provide a first overview of the simulated source behaviour at the reference plasma parameters in the absence of the magnetic field. The graphs of the electron density and, in particular, of the potential reveal that the new integration domain geometry preserves the symmetry of the solution with respect to the $y = 0$ line (top-down symmetry), symmetry which is however broken along the $x = 0.20\ m$ axis (left-right symmetry). As a matter of fact, the removal from the integration domain of the vacuum lateral zones beside the driver region introduces an element of asymmetry that can be clearly noticed. These lateral areas are not indeed represented as a part of the spatial integration domain of the simulation and therefore marked as blank rectangles. Moreover, the potential plot might suggest that the two corners marking the division between the driver and the expansion regions could be exposed to a great gradient of the potential due to their sharp geometry and any extensive and deep analysis of the neighbouring zones, which is not the scope of this thesis, should pay close attention to their influence over the proper local numerical convergence of the code. The electron temperature plot denotes instead quite a significant uniformity of T_e, with marginally higher values in the driver region where the RF power is delivered.

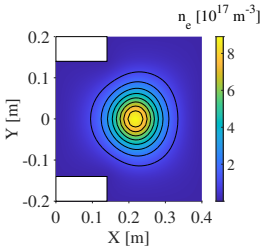

(a) n_e 2D plot, $|\boldsymbol{B}|$= 0 mT, **mesh 2**.

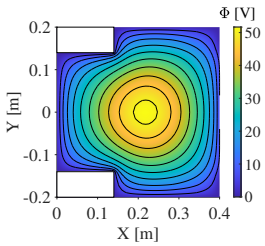

(b) Φ 2D plot, $|\boldsymbol{B}|$= 0 mT, **mesh 2**.

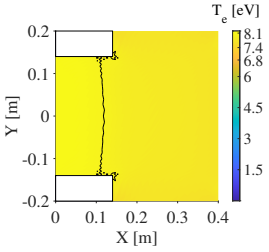

(c) T_e 2D plot, $|\boldsymbol{B}|$= 0 mT, **mesh 2**.

Figure 5.4: Reference case plots: $P_{RF} = 30\ kW/m$, $\Phi_{PG} = 5\ V$, $P = 0.3\ Pa$, $|\boldsymbol{B}|$= 0 mT, **mesh 2**.

Power scan. The results of the power scan without magnetic field are shown in 5.5. It is to be noted that resulting plasma parameters have been plotted along two orthogonal lines, as indicated beneath the graphs and marked with 2 *red* lines in figures 5.1 and 5.2. The scan explored the power range between $P_{RF} = 10\ kW/m$ and $P_{RF} = 50\ kW/m$, keeping unchanged the other parameters of the reference case. It is notable that the electron temperature is depending on the P_{RF} and quite uniform along both axes although the heating power is applied exclusively in the driver region. This is related to the high electron thermal conductivity.

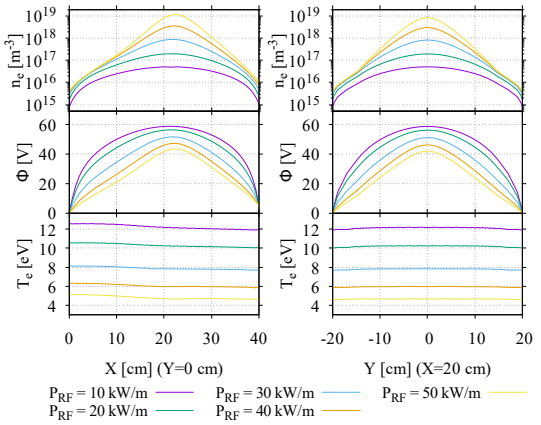

Figure 5.5: Plasma parameters for different values of P_{RF}, $|\boldsymbol{B}|= 0$ T, **mesh 2**.

It appears also evident that electron temperature decreases by a factor of 2.5 as P_{RF} increases up to 50 kW/m. That is to be attributed most probably to the fact that higher heating power allows a greater number of ionising processes which brings to an increase of the electron density. In this regard, n_e changes significantly by varying the power, about 2 orders of magnitude, reflecting a non-linear dependency of n_e on the provided power. The peak of n_e slightly moves along the x-axis toward the PG for higher values of power. It has been also found that steady-state convergent solutions exist only for values of P_{RF} at least greater than 8 kW/m but lower than 52 kW/m. Finally, the change of the potential associated to the increasing power indicates that its gradient ($|\boldsymbol{E}|= |-\boldsymbol{\nabla}\Phi|$) is reduced by the power at the walls, which is associated to the variation in the electron density rather than the electron velocity which is proportional to $\sqrt{T_e}$.

Pressure scan. The results for increasing levels of gas pressure are presented in the graphs 5.6 and range from $P = 0.2$ Pa to $P = 0.6$ Pa. The other parameters are the same as in the reference case. Higher values of gas pressure lead to a greater electron density in particular in the central region, although the increase seems to saturate for larger pressures. Instead, the electron temperature behaviour is such that T_e is reduced by the increased gas pressure. Finally, the potential tends to saturate at lower values for increasing gas pressure.

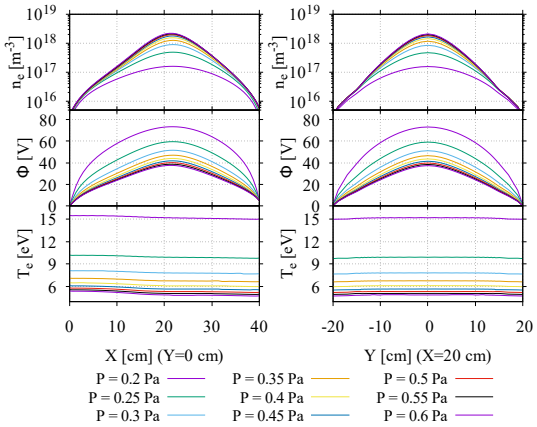

Figure 5.6: Plasma parameters for different values of P, $|\boldsymbol{B}|= 0$ T, **mesh 2**.

PG potential scan. The plots obtained letting the PG potential vary from 0 V to 50 V, keeping unchanged the other parameters, are displayed in figure 5.7. It is clear that electron temperature is poorly affected by the change of the bias potential at the plasma grid, since the resulting range of temperature variation is not greater than 1 eV. A slightly lower temperature in the expansion chamber with respect to the driver region is visible.

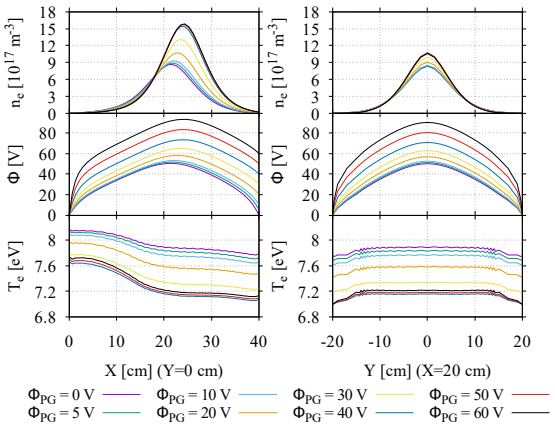

Figure 5.7: Plasma parameters for different values of Φ_{PG}, $|\boldsymbol{B}|= 0$ T, **mesh 2**.

However, these differences are quite small, never more than 0.5 eV, and are barely noticeable in the previous scans. On the other hand, n_e increases in particular along the x-axis in the expansion region for higher values of PG potential. The potential too shows a clear asymmetry along the x-direction due to the variation of PG bias potential, but the strength of the electric field, which is $|\boldsymbol{E}|= |-\boldsymbol{\nabla}\Phi|$, increases for smaller values of PG potential near the plasma grid and, vice versa, is greater at the increasing of Φ_{PG} in the driver region. It is possible to see weak fluctuations in the temperature graphs: this numerical effect will be addressed separately in section 5.1.3, where it is compared to cases involving meshes with slight changes to avoid this problem.

5.1.2 Effect of the magnetic field

Spatial distributions of the plasma parameters display a vertical asymmetry in the experiments conducted on SPIDER: this is caused by $\boldsymbol{E} \times \boldsymbol{B}$-drifts associated to the decrease of plasma potential at the source and it is induced by the magnetic filter, MF [11]. The shape and intensity of the MF strongly affect the magnitude of the asymmetry and therefore the plasma parameters. Hence, the following simulations take into account the presence of the magnetic field $\boldsymbol{B}$. In SPIDER, the MF field is produced in order to reduce the electron temperature and the quantity of plasma electrons before the PG. Consequently, the magnetic field has a rather complicated 3-D structure with a strong component in the z-direction. In order to simplify the problem, an idealised B-field of the form $\boldsymbol{B} = (B_x, B_y, B_z) = (0, 0, -B_{MF})$ is assumed in the current model. Note that the integration domain in figure 5.3 lies on the $z = 0$ plane. An analytic form of the MF profile is thus assumed instead of having the code reading as input the real MF configuration from a file [20, 11]. The B_{MF} analytic form is postulated to be a Gaussian one with the maximum B_{max} at the x_{MF} position and the width of $\sigma_{MF} = 7\,cm$:

$$B_{MF} = B_{max} \cdot exp\left[-\frac{1}{2}\left(\frac{x - x_{MF}}{\sigma_{MF}}\right)^2\right].$$

That said, the next simulations have been performed starting from the case with the same plasma parameters as the reference case of the previous paragraphs scans: RF-heating power $P_{RF} = 30\ kW/m$, gas pressure $P = 0.3\ Pa$, PG potential $\Phi = 5\ V$ and with different strength and position of the B-field maxima. The first calculations are aimed at investigating the influence of the MF field maximum position on plasma parameters and next the effect of the intensity of the field is analysed.

MF position. To analyse the effects of the change in position of the maximum of the B-field profile, the starting reference case was taken at $x_{MF} = 0.20\ m$ and $B_{max} = 4\ mT$. The scan gradually proceeded towards $x_{MF} = 0.27\ m$ by steps of $0.01\,m$ at a time. The computations converged up to the case of $x_{MF} = 0.26\ m$ and did not admit a steady solution for $x_{MF} \geqslant 0.27\ m$. A solution to that has been found by changing the minimum value that a certain parameter in the code labelled as "TT" might take. As a matter of fact, for $|\boldsymbol{B}| > 0$ and low temperatures, diffusion might be too low, leading to numerical problems. A parameter TT is consequently introduced in the FSFS2D code, such that if $T_e \geqslant 2\ eV \ \Rightarrow\ \mathrm{TT} = 1$, and TT increases strongly for $T_e < 2\ eV$.

More exactly TT is defined as $\mathrm{TT} = min\left\{\left(\frac{max\{2\ eV,\ T_e\}}{T_e}\right)^4,\ a\right\}$,

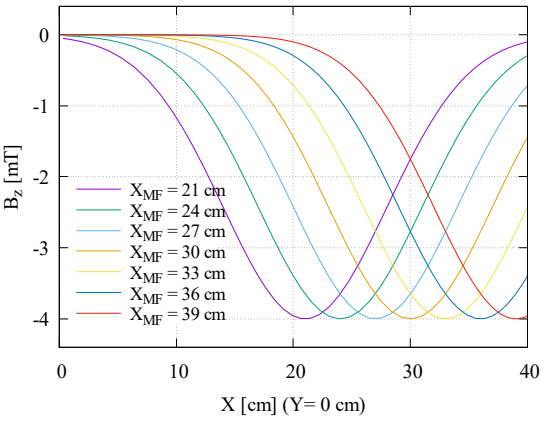

Figure 5.8: B_z profiles for different values of x_{MF}.

where $a = 10^3$ was used in all previous simulations. The solution to the problem consists in lowering it to 10^2, which means setting the minimum value that TT can take to 10^2 instead of 10^3. TT is used as a multiplicative factor, if temperature is too low, purposely inserted in to diffusion coefficient D_e to create "artificial diffusion" which is needed for the numerical method to correctly work. The reason of that lies in the fact that great variations of $|\boldsymbol{B}|$ give great changes of D_e in minimal distances: within 3 or 4 points in the mesh it decreases by 3 orders of magnitude and therefore the diffusion equations are numerically difficult to be solved. Indeed, one may note that the decreasing $|\boldsymbol{B}|$ field lowers μ_e (mobility coefficient) and T_e, but $D_e \propto \mu_e\, T_e$. The TT recalibration is thus strictly related to the B_z field profile and functional to these cases (from $x_{MF} = 0.27\ m$ to $x_{MF} = 0.39\ m$). Once operated this change, the results for fixed $B_{max} = 4\ mT$, $\sigma_{MF} = 7\ cm$ and higher x_{MF} have been found for all considered x_{MF} range. Corresponding B_z profiles are presented in figure 5.8. The simulations results for selected x_{MF} positions are shown in fig.5.9.

It turned out that potential is weakly affected by the position of the B-field maximum: a slight shift of Φ maximum towards the PG as x_{MF} increases is just noticeable. On the other hand, n_e seems to follow the MF as it moves towards the driver, increasing its peak up to two times when the field enters more deeply into the driver. Also the electron temperature profiles are quite influenced by the change in x_{MF} position. It is indeed quite reduced in the expansion chamber and near its walls when the MF is closer to the driver region, although the temperature inside the driver region itself and immediately before the PG remains almost unchanged.

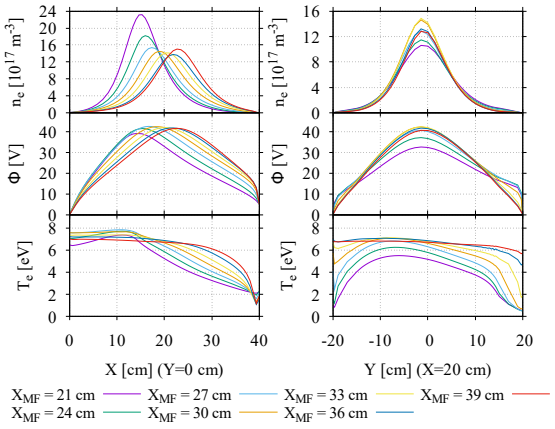

Figure 5.9: Plasma parameters for different values of x_{MF}, $\boldsymbol{B_{max} = 4\ mT}$, $P_{RF} = 30\,kW/m$, $P = 0.3\,Pa$, $\Phi_{PG} = 5\,V$, **mesh 2**.

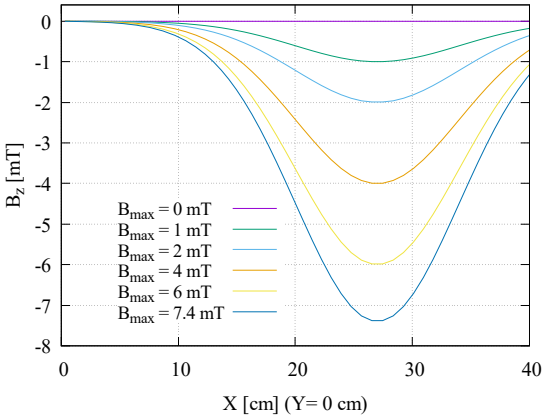

Figure 5.10: B_z profiles for different values of B_{max}.

Varying B-field intensity. The results having the B_{max} varying up to 7.4 mT are shown in fig. 5.11. The position of the B-field maximum is fixed at $x_{MF} = 0.27\ m$, see fig. 5.10. The other plasma parameters have the same fixed values as the reference case in sec. 5.1.1: $P_{RF} = 30\,kW/m$, $\Phi_{PG} = 5\,V$ and $P = 0.3\,Pa$.

Fig. 5.11 shows that the increase of the magnetic field induces a growth in electron density, from $\sim 9 \cdot 10^{17}\ m^{-3}$ to $\sim 20 \cdot 10^{17}\ m^{-3}$ and a slight shift of the peak toward the driver region. A little y-axis profile asymmetry of n_e may be seen, weakly growing with the B_{max} value. Regarding the electron temperature, the plots indicate a considerable diminution of the temperature in the expansion chamber as much as PG is approached; T_e is instead almost unaffected in the driver region. A reduction is also observed close to the expansion chamber walls along y-axis, with some irregularities that can be attributed to some numerical issues in the definition of the boundary conditions, especially for $y = -0.20\ m$, which may be solved by a finer mesh resolution.

It results that potential is weakly affected by the variation of the intensity of the field, with a little growth in asymmetry as the field increases. Moreover, the potential is reduced more significantly for larger values of position along the y-axis and its profile along this axis presents a marked drop close to the wall, in particular as the intensity of the field grows.

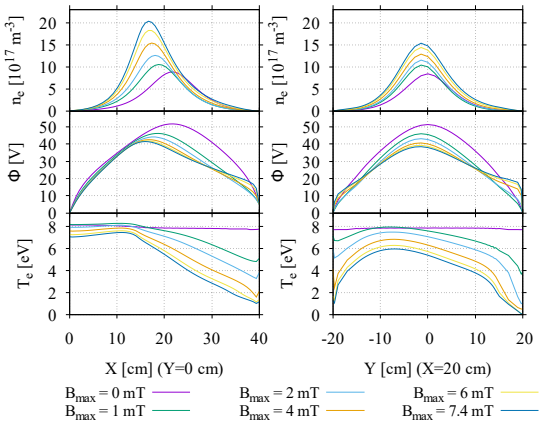

Figure 5.11: Plasma parameters for different values of B_{max}, **mesh 2**.

Overall behaviour, $\boldsymbol{B_{max} = 4\ mT}$. In the figure 5.12, plots analogous to those in 5.4 can be seen. This time, reference case plasma parameters are set at the same values as in section 5.1.1, but magnetic filter is now considered with the following parameters: $B_{max} = 4\ mT$ and $x_{MF} = 0.39\ m$. The same values of B-field are used in the power, pressure and potential scans shown in the next paragraphs. Note, that the value of x_{MF} has been chosen in accordance with the value used for mesh 1 [20]. The 2-D plots show important effects of the B-field on plasma parameters. The top-down symmetry of the electron density is broken due to the presence of drifts as illustrated also in the previous paragraph. Moreover, the peak of n_e increases from $\sim 8 \cdot 10^{17}\ m^{-3}$ to $\sim 15 \cdot 10^{17}\ m^{-3}$ with the MF; the value of the potential maximum is instead lower in the presence of the B-field.

An important change is observed for the electron temperature that drastically drops around the position of $x = 30\ cm$, with a consequent reduction in electron thermal conductivity[1]. It should be highlighted that the drop in temperature occurs more distant from the PG (and therefore x_{MF}) along the lateral walls of the chamber with respect to smaller y-coordinate positions. This means that T_e falls for lower values of x on the walls of the EC.

$B_{max} = 4\ mT$, RF power scan. The three scans from section 5.1.1 have been repeated to check the influence of the MF on the plasma parameters at fixed $x_{MF} = 0.39\ m$ and $B_{max} = 4\ mT$, using the same other parameters as in the reference case (see section 5.1.1). The power scan shows similar results with respect to the analogous one with $|\boldsymbol{B}| = 0$, although the simulations provided convergent solutions only for P_{RF} between 14 kW/m and 47.5 kW/m (only cases with P_{RF} values analogous with mesh 1 are presented in fig. 5.13 for further comparisons in section 5.2). Electron density increases and its peak shifts toward the PG with a significant gradient near it as the power raises, T_e instead drops notably close to the PG, in particular for lower values of power.

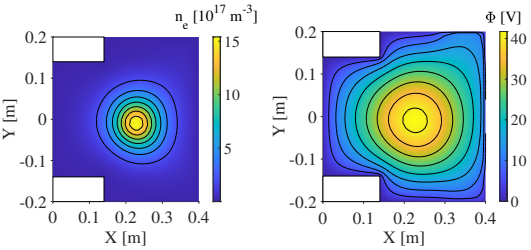

(a) n_e 2D plot, $B_{max} = 4\ mT$, **mesh 2**.

(b) Φ 2D plot, $B_{max} = 4\ mT$, **mesh 2**.

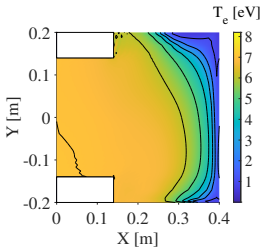

(c) T_e 2D plot, $B_{max} = 4\ mT$, **mesh 2**.

Figure 5.12: Reference case plots: $P_{RF} = 30\ kW/m$, $\Phi_{PG} = 5\ V$, $P = 0.3\ Pa$, $x_{MF} = 0.39\ m$ $B_{max} = 4\ mT$, **mesh 2**.

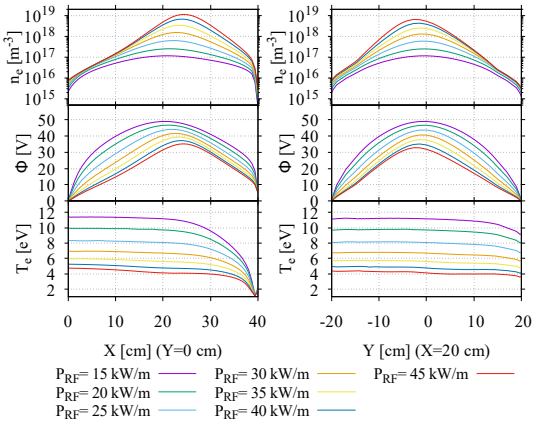

Figure 5.13: Plasma parameters for P_{RF} scan, $B_{max} = 4\ mT$, **mesh 2**.

$B_{max} = 4\ mT$, pressure scan. The results for the scan at different levels of gas pressure (other reference parameters are not changed) are presented in figure 5.14 and reveal a similar behaviour with respect to the ones in the absence of magnetic field. The increase of pressure induces a greater electron density and a slight shift to the driver region with a general saturation effect for n_e, Φ and T_e. Φ tends to be reduced for higher pressure just like electron temperature, which is reduced significantly at the plasma grid and weakly along y-axis close to $y = 0.20\ m$. The range of pressure values within which the computations give self-consistent solutions is between 0.225 Pa and 0.6 Pa, although only the results corresponding to the analogous cases in mesh 1 are shown.

$B_{max} = 4\ mT$, PG potential scan. The graphs of the results of the simulations for different values of PG potential are in fig. 5.15 (other input parameters correspond to the reference case). Compared to the cases without the MF, the electron density appears much increased by greater potentials that make its peak move toward the PG. Also Φ is decisively increased for growing values of Φ_{PG} especially in the expansion chamber. The electron temperature is lower for increasing PG potential values in both driver region and expansion chamber, but the trend changes just next to the PG where the opposite is true. Conversely, along the y-axis it is weakly influenced by PG potential but tiny

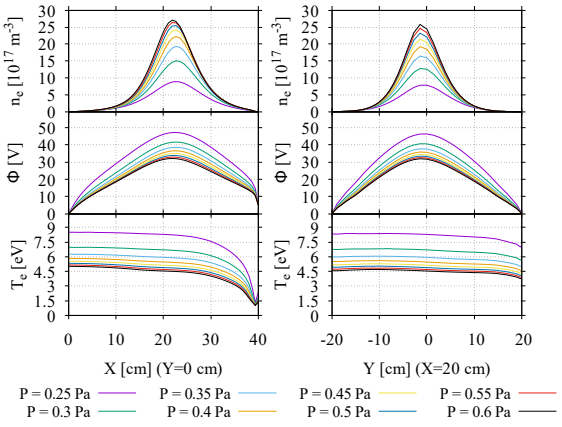

Figure 5.14: Plasma parameters for P scan, $B_{max} = 4\ mT$, **mesh 2**.

[1] To be noted that $\hat{\boldsymbol{\chi}}_e = \frac{5}{2}\hat{\boldsymbol{\mu}}_e T_e$ [20, 7], see section 2.4

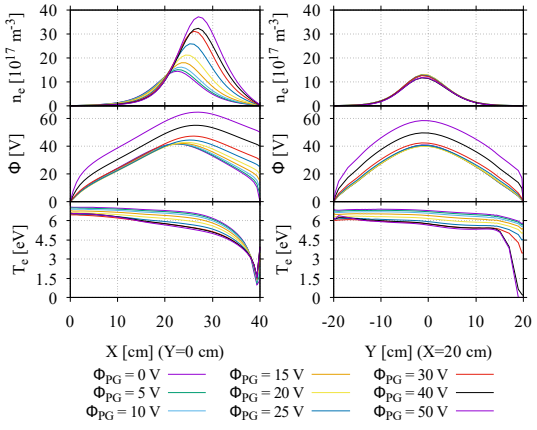

Figure 5.15: Plasma parameters for Φ_{PG} scan, $B_{max} = 4\ mT$, **mesh 2** and **mesh 2 new**.

reduction as Φ_{PG} increases, limited to values strictly less than $\Phi_{PG} = 40\,V$. From this values upwards simulations gave problematic solutions near the upper border of the expansion chamber, that will be later addressed (the results corresponding to the last two values of PG potential have been calculated using a different mesh, **"mesh 2 new"**, see next section for details).

5.1.3 Mesh changes due to the presence of the magnetic field

As mentioned before, a slightly modified mesh 2 has been used for the last two cases of the PG potential scan with the MF. This was necessary in order to obtain a convergent solution for $\Phi_{PG} = 40\,V$ or above. So as to discuss these changes, a more precise description of mesh 2 (fig. 5.2) is required.

Mesh 2, points along x-axis. The following parameters are defined: the total mesh x-axis length l_x, the driver region x-axis length $d_{d,x}$, the expansion chamber x-axis length $d_{e,x}$.
The number of points along x-direction in the driver region is $N_{d,x} = N_{tot,x} \cdot d_{d,x}/l_x$. Analogously, for the expansion chamber EC it is $N_{e,x} = N_{tot,x} - N_{d,x}$.
The density of points is symmetrical with respect to $x = d_{d,x}/2$ in the driver: greater density near the wall and at the contact region between driver zone and EC. In the EC points along x axis are symmetrical with respect to the middle of the expansion zone, preserving the continuity of the mesh step at the interface between the driver region and the expansion chamber.

Mesh 2, points along y-axis. The source can be divided along the y-axis in a central region (Y-DB) and a couple of lateral regions (Y-LECB and Y-UECB).
The code requires the Y-DB number of points ($N_{d,y}$) to be defined and then it calculates the correspondent Y-DB distribution, symmetrical with respect to the line $y = 0$. Finally, the code computes the Y-LECB and Y-UECB symmetrical distribution using $N_{tot,y} - N_{d,y}$ points, with clear meaning of the symbols. The program also fixes the border conditions to have continuity in the regions between the three bands and lower density in the middle of Y-DB and each Y-LECB and Y-UECB separately.

Mesh 2 new. A new mesh is now defined, that shall be called "mesh 2 new", with the same overall configuration principles but few little changes.
In the mesh 2 the Y-LECB and Y-UECB regions have a number of points proportional to their length, but in "mesh 2 new" if the number of points along the y-axis

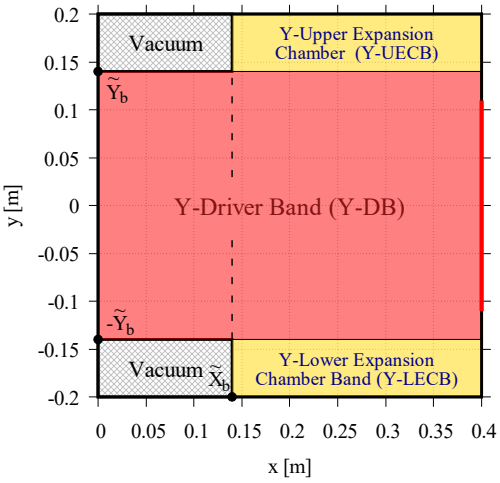

Figure 5.16: Representation of the source seen as y-bands.

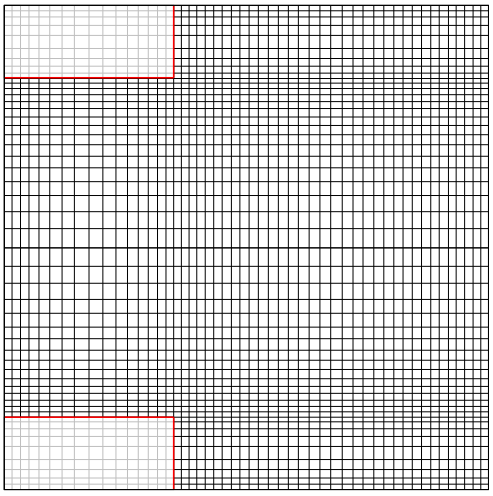

Figure 5.17: Representation of the "mesh 2 new".

in at least one of the two lateral bands is less than $N_{tot}/5$, then the number is set to $N_{tot}/5$ in each of them, whereas $3N_{tot}/5$ points will be assigned to the Y-DB. Some simulations are shown to illustrate the results with the use of "mesh 2 new".

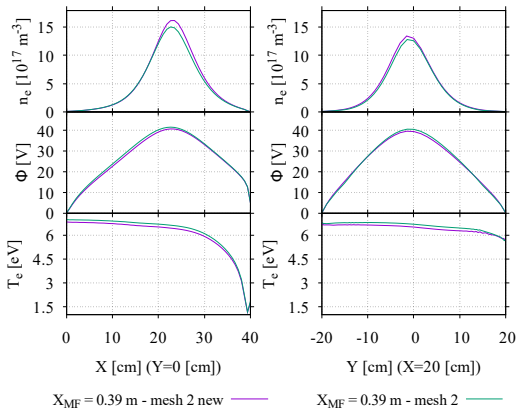

Figure 5.18: Comparison mesh 2 - mesh 2 new, $B_{max} = 4\ mT$, $P_{RF} = 30\ kW/m$, $\Phi_{PG} = 5\,V$, $P = 0.3\ Pa$, $x_{MF} = 39\,cm$.

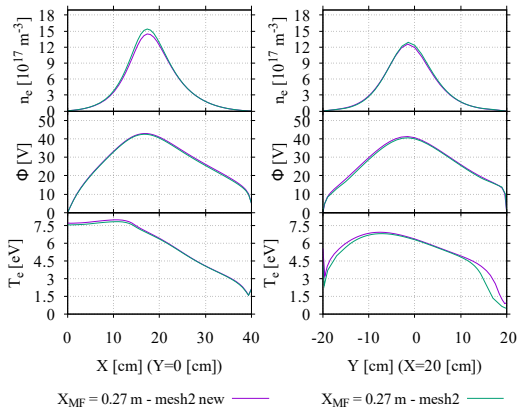

Figure 5.19: Comparison mesh 2 - mesh 2 new, $B_{max} = 4\ mT$, $P_{RF} = 30\ kW/m$, $\Phi_{PG} = 5\,V$, $P = 0.3\ Pa$, $x_{MF} = 39\,cm$.

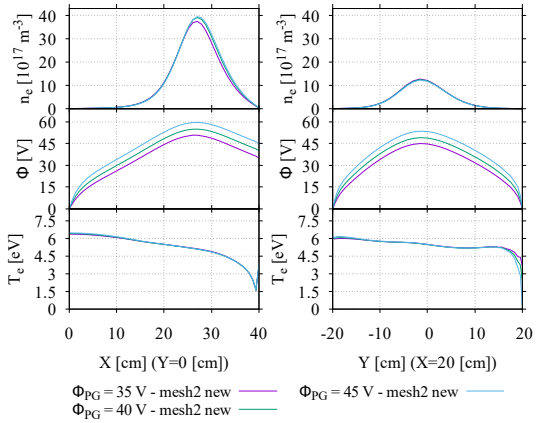

Figure 5.20: Plasma parameters for high PG potential mesh 2 new, $B_{max} = 4\ mT$, $P_{RF} = 30\ kW/m$, $P = 0.3\ Pa$, $\Phi_{PG} = 5\,V$, $x_{MF} = 0.39\ m$.

Figs. 5.18 and 5.19 show that with "mesh 2 new" the code produces the same results as with mesh 2 in the cases for which a steady-state solution is obtained with the latter. To be accurate, for the case $x_{MF} = 0.27\ m$, the electron temperature near the upper wall in the EC appears slightly higher when mesh 2 new is employed (fig. 5.19). However, for higher values of Φ_{PG}, convergent solutions can be found only with the mesh 2 new due to the mentioned numerical instability (fig. 5.20).

It should be noted, that numerical methods using high order schemes, although giving at least theoretically better approximations, can lead to some sort of oscillation tendencies [15]. To show this behaviour, a 5-points-scheme simulation with mesh 2 and no B-field has been performed (instead of a 9-points-scheme one, as described in chapter 3), and no oscillation was found in electron temperature profiles, fig. 5.21.

As a matter of fact, not only the 9-points-scheme should give better results, but if B-field is present the 5-points one can not even be used.
However, in the absence of the magnetic field there are no corresponding drifts and consequently no mixed partial derivatives of the form $\frac{\partial^2 f}{\partial x \partial y}$ must be numerically calculated. Thus, the 5-points-scheme is exploitable. It comes out, at least in the current implementation of the numerical method, that 5-points-scheme ensures more numerical stability.

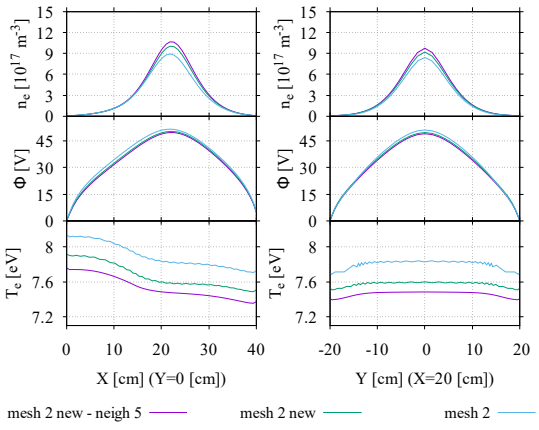

Figure 5.21: Comparson 9&5-points-scheme, $B_{max} = 0\ mT$, $P_{RF} = 30\ kW/m$, $\Phi_{PG} = 5\,V$, $P = 0.3\ Pa$.

5.1.4 3-dimensional plots in mesh 2

On page 19, some 3-dimensional graphs are displayed just as reference, giving a general overview and a better comparison between the cases already illustrated in figures 5.4 and 5.12.

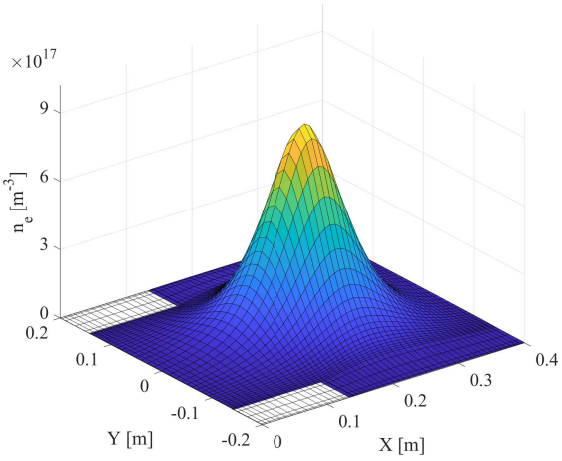

Figure 5.22: n_e 3D plot, $P_{RF} = 30\ kW/m$, $\Phi_{PG} = 5\ V$, $P = 0.3\ Pa$, $|\boldsymbol{B}| = 0\ mT$, **mesh 2**.

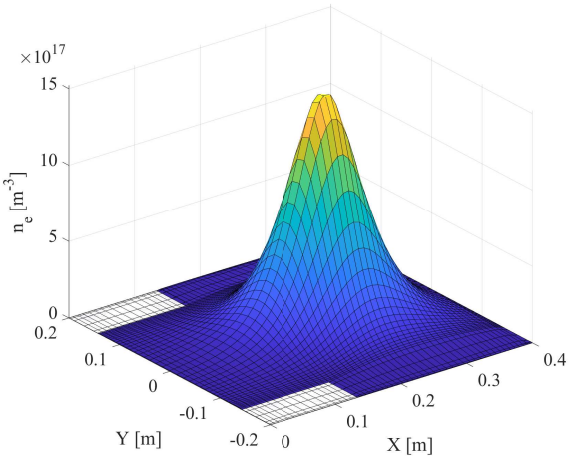

Figure 5.25: n_e 3D plot, $P_{RF} = 30\ kW/m$, $\Phi_{PG} = 5\ V$, $P = 0.3\ Pa$, $x_{MF} = 0.39\ m$ $B_{max} = 4\ mT$, **mesh 2**.

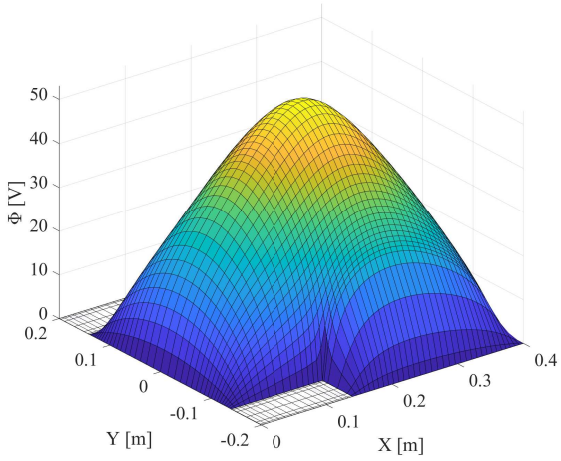

Figure 5.23: Φ 3D plot, $P_{RF} = 30\ kW/m$, $\Phi_{PG} = 5\ V$, $P = 0.3\ Pa$, $|\boldsymbol{B}| = 0\ mT$, **mesh 2**.

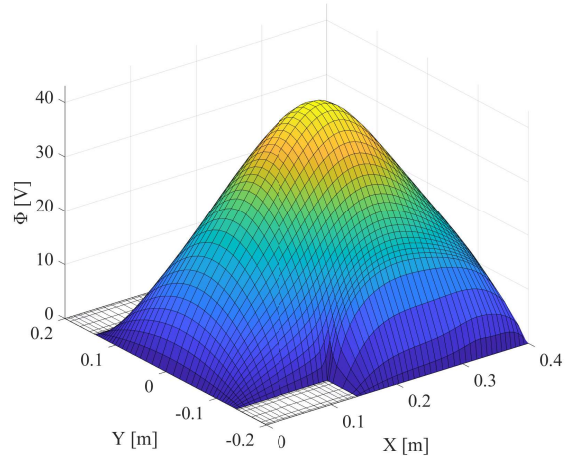

Figure 5.26: Φ 3D plot, $P_{RF} = 30\ kW/m$, $\Phi_{PG} = 5\ V$, $P = 0.3\ Pa$, $x_{MF} = 0.39\ m$ $B_{max} = 4\ mT$, **mesh 2**.

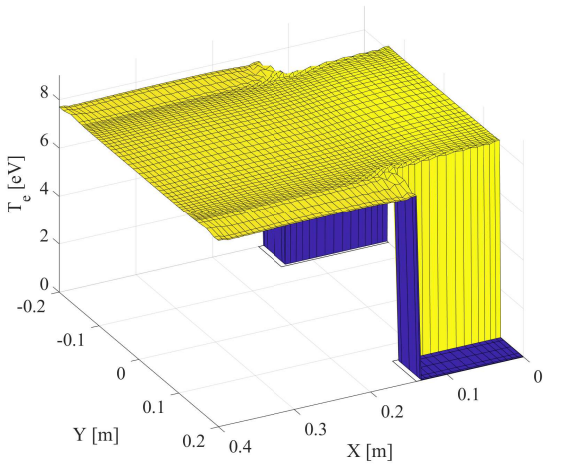

Figure 5.24: T_e 3D plot, $P_{RF} = 30\ kW/m$, $\Phi_{PG} = 5\ V$, $P = 0.3\ Pa$, $|\boldsymbol{B}| = 0\ mT$, **mesh 2**.

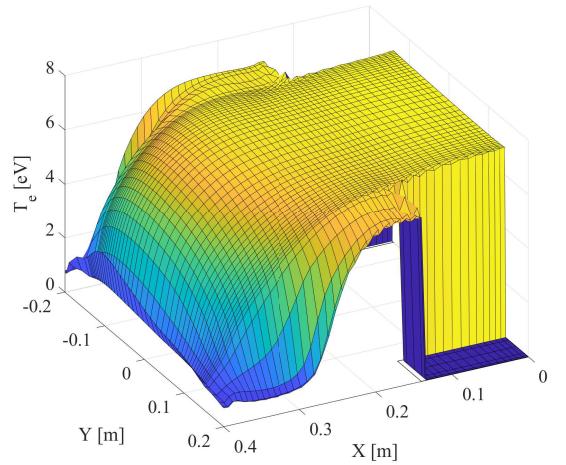

Figure 5.27: T_e 3D plot, $P_{RF} = 30\ kW/m$, $\Phi_{PG} = 5\ V$, $P = 0.3\ Pa$, $x_{MF} = 0.39\ m$ $B_{max} = 4\ mT$, **mesh 2**.

5.2 Comparisons between different geometries

The results presented in the section 5.1 (above) are here briefly compared to those computed using the ***mesh 1*** (fig. 5.28). The parameters of the reference cases from which the scan results have been obtained are the same as those employed with ***mesh 2*** (see sec. 5.1.1): including the applicable magnetic filter with $B_{max} = 4\ mT$, $x_{MF} = 0.39\ m$ and $\sigma_{MF} = 7\ cm$.

5.2.1 Mesh 1 - cases without B-field

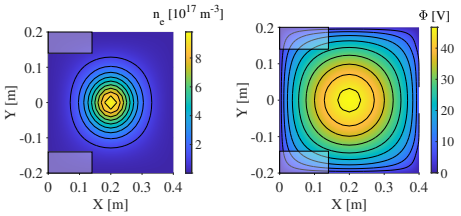

(a) n_e 2D plot, $B_{max} = 4\ mT$, **mesh 1**.

(b) Φ 2D plot, $B_{max} = 4\ mT$, **mesh 1**.

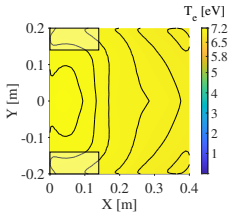

(c) T_e 2D plot, $B_{max} = 4\ mT$, **mesh 1**.

Figure 5.28: Reference case plots: $P_{RF} = 30\ kW/m$, $\Phi_{PG} = 5\ V$, $P = 0.3\ Pa$, $|\boldsymbol{B}| = 0\ mT$, **mesh 1**.

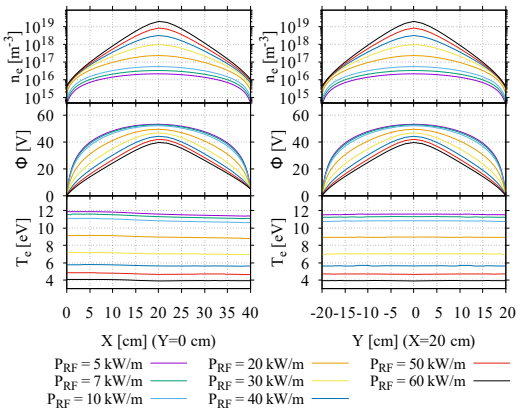

Figure 5.29: Plasma parameters for RF power scan, $|\boldsymbol{B}| = 0\ mT$, **mesh 1**.

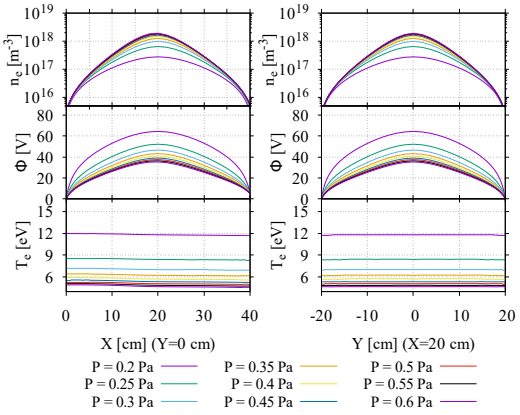

Figure 5.30: Plasma parameters for pressure scan, $|\boldsymbol{B}| = 0\ mT$, **mesh 1**.

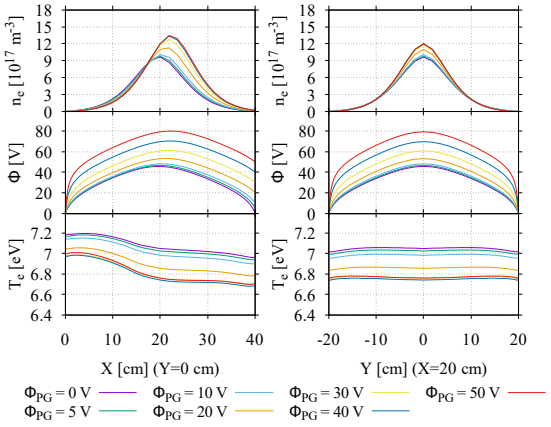

Figure 5.31: Plasma parameters for PG potential scan, $|\boldsymbol{B}| = 0\ mT$, **mesh 1**.

The maps in fig. 5.28 illustrate the representative steady-solution without B-field: both n_e and Φ differ from those in fig. 5.4 (mesh 2) presenting a perfect symmetry in both directions. In addition, heat can be seen transferred also into the regions, labelled as "VZs", that were empty in mesh 2 (they are here marked for reference). Moreover, fig. 5.29 shows a symmetric n_e profile along x-axis, contrary to the asymmetry observed for mesh 2 due to imposed vacuum regions. In contrast to mesh 1, the power scan of mesh 2 gives n_e profile along y-direction decreasing sharply in the shadow of the VZs, as if slightly screened from the power source by the VZs (see e.g. fig. 5.5). It is noticeable also that the temperature tends to saturate as a function of P_{RF}, which may be due to numerical issues. In general, mesh 1 T_e seems overall slightly lower in each of the 3 scans, e.g. in mesh 1 for $P = 0.6\ Pa$, $T_e \sim 12\ eV$ in spite of $T_e \sim 15\ eV$ recorded for mesh 2. Also, in fig. 5.31 at $\Phi_{PG} = 50\ V$, n_e peak is remarkably lower: in mesh 1 $n_e^{max} \lesssim 14 \cdot 10^{17}\ m^{-3}$, whereas $n_e^{max} \sim 16 \cdot 10^{17}\ m^{-3}$ in mesh 2.

5.2.2 Mesh 1 - case with B-field

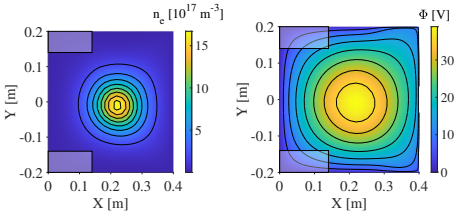

(a) n_e 2D plot, $B_{max} = 4\ mT$, **mesh 1**.

(b) Φ 2D plot, $B_{max} = 4\ mT$, **mesh 1**.

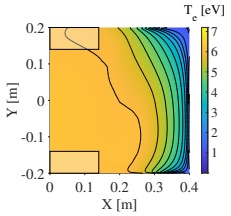

(c) T_e 2D plot, $B_{max} = 4\ mT$, **mesh 1**.

Figure 5.32: Reference case plots: $P_{RF} = 30\ kW/m$, $\Phi_{PG} = 5\ V$, $P = 0.3\ Pa$, $x_{MF} = 0.39\ m$ $B_{max} = 4\ mT$, **mesh 1**.

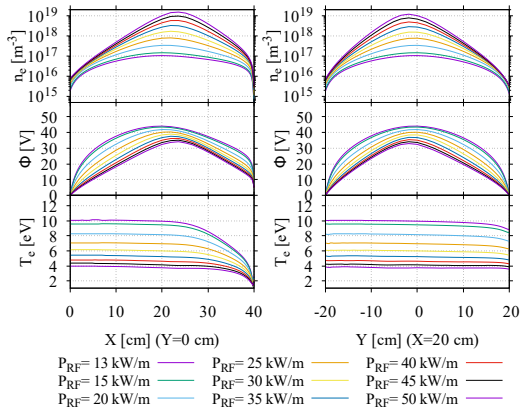

Figure 5.33: Plasma parameters for RF power scan, $B_{max} = 4\ mT$, **mesh 1**.

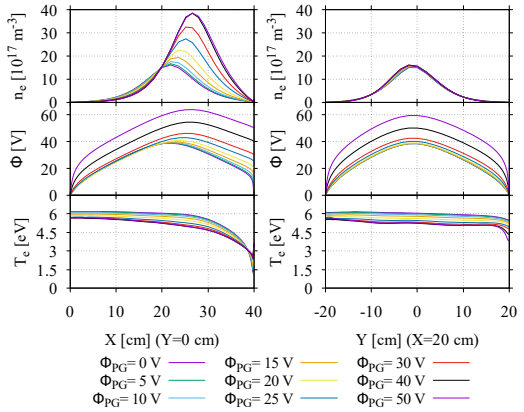

Figure 5.34: Plasma parameters for PG potential scan, $B_{max} = 4\ mT$, **mesh 1**.

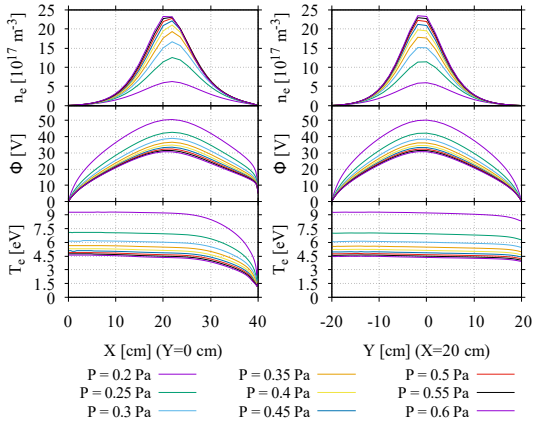

Figure 5.35: Plasma parameters for pressure scan, $B_{max} = 4\ mT$, **mesh 1**.

In fig. 5.32 the first two plots (n_e and Φ) exhibit a little asymmetry with respect to the $x = 0.2\ m$ line, induced by the MF. The latter is predominantly deformed in correspondence of $x_{MF} = 0.39\ m$, just like for mesh 2, see fig. 5.12. On the other hand, mesh 1 T_e map shows a clearer, sharper, drop for MF maximum position compared to the mesh 2 one, especially along the EC walls. Once again, it is recognisable that T_e is overall higher ($\sim 1\ eV$ on average) in both directions at fixed scan parameters for mesh 2, if compared to mesh 1, see fig. 5.33 to 5.35. This may be associated to the fact that in the former case the heat is transferred only to the EC and not also to the VZs. The same differences in behaviour between mesh-1 and mesh-2 cases can be spotted for n_e and T_e in the power scan, in analogy to the corresponding result without $\boldsymbol{B}$-field. On the other hand, mesh 1 Φ and T_e profile shapes result to strongly agree to those of mesh 2. Concerning the potential scan, mesh 1 might turn out to be more numerically stable along y-axis for $y \sim 0.2\ m$: there T_e keeps being relatively high with just a tendency to lower close to the upper wall ($y > 0$) for higher values of Φ_{PG}. Mesh 2 showed instead some issues for $\Phi_{PG} = 40\ V$ and $50\ V$, with a significant T_e drop. Finally, pressure scan reported lower n_e peaks at fixed P for mesh 1, but slightly higher Φ gradient (so E-field values) at the EC walls with respect to mesh 2 correspondent case.

5.2.3 Comparisons between mesh 1 and mesh 2 in the driver region

In this paragraph, a further profile comparison between the two meshes is presented. As a matter of fact, all the previous profile plots represented plasma parameters as a function of one spatial coordinate at fixed value of the other, $y = 0\ m$ in one case and $x = 0.2\ m$ for the other one. Therefore, the y-profiles with fixed $x = 0.2\ m$ referred only to the EC whereas the plots along the $y = 0$ line displayed the driver region just for the first 14 cm. In order to better compare the behaviour of those quantities in the driver region, the following profiles have been made along the $x = 0.07\ m$ line, as indicated by the vertical *blue* lines in fig. 5.1 and fig. 5.2. For this purpose, it has been chosen to represent and compare n_e and T_e at $x = 0.07\ m$ profiles for the above-mentioned reference cases with the magnetic field or in the absence of it, both for **mesh 1** and **mesh 2**.

Electron density, driver region. The plots on the left-hand side of fig. 5.36 show the electron density with the MF (lower one) and without MF (upper one) in the middle of the driver region and in parallel to the y-axis. It must be pointed out that the real driver region is the one defined for values of y between $y_1 = -0.14\ m$ and $y_2 = 0.14\ m$. The intervals outside this range correspond to the vacuum zones (VZs), in which only mesh 1 plots show non-zero values of electron density due to the fact that simulations conducted in the simplified rectangular geometry included the VZs as parts of the integration domain. As a matter of fact, the symmetric shape of the electron density profile observed for mesh 1 is analogous to the shape exhibited in the EC[2], although the value of the maximum is considerably reduced, whether the MF is present or not. The reason of that is found in fig. 5.28a, showing that electron density is much grater in the centre of the EC. To the other hand, the profiles for mesh 2 totally drop at the limits of the driver region. It is interesting to notice also that in general n_e is a little lower with respect to the case with mesh 1.

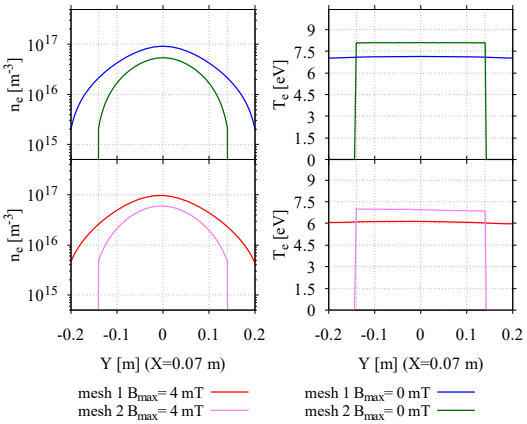

Figure 5.36: n_e and T_e driver profiles ($x = 0.07\ m$), $B_{max} = 0\ mT$ and $B_{max} = 4\ mT$, **mesh 1** and **mesh 2** comparisons.

Electron temperature, driver region. Analogously to density, electron temperature shows a rapid drop close to the driver walls for mesh 2, whereas T_e is almost uniform along the $x = 0.07\ m$ line of mesh 1. However, despite the fact that mesh-1-n_e is overall higher with respect to the results of the other mesh, for the electron temperature is true the opposite: T_e computed in mesh 2 is some 1 eV greater than T_e in mesh 1 inside the driver region and falls to zero outside of it. Finally, the presence of the magnetic filter does not alter particularly the shape of the profiles, besides slightly lowering them, in agreement with the fact that the MF is not intended to penetrate into the driver region as reported in [20].

[2] See the right-hand side of fig. 5.29 and fig. 5.33.

Chapter 6

Conclusions

A self-consistent fluid model description of a low-pressure discharge has been presented within a two-dimensional section of one of the eight driver volumes, including the expansion chamber, that make up SPIDER negative ion source. This model employs different continuity equations for each of the particle species involved with the assumption of the drift-diffusion approximation for particle fluxes. Electron temperature is obtained by the electron energy balance equation whereas the neutral species and ions are assumed to have uniform and constant temperatures. Finally, the electrostatic coupling between electrons and ions is described by the Poisson equation. The numerical method is based on finite volume approximation and 9-point discretisation on a two-dimensional staggered mesh is used in order to take into account the anisotropy due to the magnetic field. The modified Poisson equation is numerically solved by means of a semi-implicit prediction of the space charge density for every mesh point [7, 11]. The model and the numerical method have been implemented in the FORTRAN 95 code FSFS2D and tested in a simplified rectangular geometry [20].

The work behind this thesis consisted of using the code to simulate and examine the behaviour of the plasma parameters in the source, in particular, the plasma potential, electron temperature and density for different values of RF-power, pressure and PG bias potential. These simulations have been performed for the first time in a more realistic SPIDER geometry and mesh, considering the vacuum zones outside the driver. This study provides an important insight of the physics of the source and gives indications for further improvements of the model and code applications.

The code predictions for the electron density, the plasma potential and the electron temperature in SPIDER geometry show general correspondence to the physical expectations and other simulations [7, 11, 20]. The results also suggest an overall agreement between the plasma parameter profiles obtained with the SPIDER mesh and the previous simulations with the rectangular mesh. However, it should be said that some numerical instability and convergency issues have been faced in the case of SPIDER-like mesh, e.g. at high PG potential ($\Phi_{PG} \gtrsim 40\ V$) in the presence of the magnetic filter field. This gave space and opportunity for a further development and improvement of the mesh in order to overcome some instabilities and enhance convergence efficiency, as presented for the new mesh, labelled "mesh 2 new". Moreover, overall physically consistent and stable numerical results are noticed in the driver region where most of the differences between the results with the two meshes were expected to occur. For instance, a uniform temperature in the driver region for the SPIDER mesh is shown, both in the presence and in the absence of the MF, with a sharp drop in the lateral vacuum zones, whereas using the rectangular mesh no distinction is made for these different regions in temperature profiles. In general, lower electron temperatures can also be observed for the SPIDER-like geometry with respect to the rectangular case. On the other hand, in the presence of the MF field, the temperature reduction still takes place close to the PG in SPIDER geometry, even though, the drop is not as clear and sharp as it was in the results of the rectangular mesh, in particular near the walls of the expansion chamber.

The future work and developments might take in consideration the comparison of the results presented above to the experimental data taken directly from the physical source through a campaign of measurements. Also, an implementation of the RF-inductive field description accounting for the coupling with fluid equations is expected to be developed and implemented in the near future [20].

Bibliography

[1] P. Agostinetti et al. "Detailed design optimization of the MITICA negative ion accelerator in view of the ITER NBI". In: *Nuclear Fusion* 56.1 (Dec. 2015), p. 016015. DOI: 10.1088/0029-5515/56/1/016015. URL: https://dx.doi.org/10.1088/0029-5515/56/1/016015.

[2] P. Agostinetti et al. "Physics and engineering design of the accelerator and electron dump for SPIDER". In: *Nuclear Fusion* 51.6 (Apr. 2011), p. 063004. DOI: 10.1088/0029-5515/51/6/063004. URL: https://dx.doi.org/10.1088/0029-5515/51/6/063004.

[3] S. I. Braginskii. "Transport Processes in a Plasma". In: *Rev. Plasma Phys.* 1 (1965), p. 205.

[4] Ian G. Brown. "Elementary Ion Sources". In: *The Physics and Technology of Ion Sources*. John Wiley & Sons, Ltd, 2004. Chap. 3, pp. 29–40. ISBN: 9783527603954. DOI: https://doi.org/10.1002/3527603956.ch3. eprint: https://onlinelibrary.wiley.com/doi/pdf/10.1002/3527603956.ch3. URL: https://onlinelibrary.wiley.com/doi/abs/10.1002/3527603956.ch3.

[5] G Fubiani et al. "Modeling of plasma transport and negative ion extraction in a magnetized radio-frequency plasma source". In: *New Journal of Physics* 19.1 (Jan. 2017), p. 015002. DOI: 10.1088/1367-2630/19/1/015002. URL: https://dx.doi.org/10.1088/1367-2630/19/1/015002.

[6] S. Günter et al. "Modelling of heat transport in magnetised plasmas using non-aligned coordinates". In: *Journal of Computational Physics* 209.1 (2005), pp. 354–370. ISSN: 0021-9991. DOI: https://doi.org/10.1016/j.jcp.2005.03.021. URL: https://www.sciencedirect.com/science/article/pii/S0021999105001373.

[7] G J M Hagelaar, G Fubiani, and J-P Boeuf. "Model of an inductively coupled negative ion source: I. General model description". In: *Plasma Sources Science and Technology* 20.1 (Jan. 2011), p. 015001. DOI: 10.1088/0963-0252/20/1/015001. URL: https://dx.doi.org/10.1088/0963-0252/20/1/015001.

[8] G. J. M. Hagelaar, F. J. de Hoog, and G. M. W. Kroesen. "Boundary conditions in fluid models of gas discharges". In: *Phys. Rev. E* 62 (1 July 2000), pp. 1452–1454.

[9] G.J.M. Hagelaar. "Modeling of microdischarges for display technology". English. PhD thesis. Applied Physics, 2000. ISBN: 90-386-1659-7. DOI: 10.6100/IR538700.

[10] Allan J. Lieberman Michael A.and A J Lichtenberg. *Principles of Plasma Discharges and Materials Processing*. John Wiley & Sons, Ltd, 2005. ISBN: 9780471724254. URL: https://onlinelibrary.wiley.com/doi/abs/10.1002/0471724254.

[11] S Lishev et al. "Fluid-model analysis on discharge structuring in the RF-driven prototype ion-source for ITER NBI". In: *Plasma Sources Science and Technology* 27.12 (Dec. 2018), p. 125008. DOI: 10.1088/1361-6595/aaf536. URL: https://doi.org/10.1088/1361-6595/aaf536.

[12] K. W. Morton and D. F. Mayers. *Numerical Solution of Partial Differential Equations: An Introduction*. 2nd ed. Cambridge University Press, 2005. DOI: 10.1017/CBO9780511812248.

[13] Suhas V Patankar. *Numerical heat transfer and fluid flow*. Series on Computational Methods in Mechanics and Thermal Science. Hemisphere Publishing Corporation (CRC Press, Taylor & Francis Group), 1980. ISBN: 978-0891165224. URL: http://www.crcpress.com/product/isbn/9780891165224.

[14] "Plasma Dynamics". In: *Principles of Plasma Discharges and Materials Processing*. John Wiley & Sons, Ltd, 2005. Chap. 4, pp. 87–132. ISBN: 9780471724254. DOI: https://doi.org/10.1002/0471724254.ch4. eprint: https://onlinelibrary.wiley.com/doi/pdf/10.1002/

0471724254.ch4. URL: https://onlinelibrary.wiley.com/doi/abs/10.1002/0471724254.ch4.

[15] D.C. Potter. *Computational Physics*. A Wiley-Interscience publication. J. Wiley & Sons, 1980. URL: https://books.google.it/books?id=qer4vgEACAAJ.

[16] Jesse Soewito Santoso. "Production of Negative Hydrogen Ions in a High-Powered Helicon Plasma Source". PhD thesis. College of Science, Research School of Physics and Engineering, Plasma Research Laboratory, 2018.

[17] E. Sartori et al. "First operations with caesium of the negative ion source SPIDER". In: *Nuclear Fusion* 62.8 (June 2022), p. 086022. DOI: 10.1088/1741-4326/ac715e. URL: https://dx.doi.org/10.1088/1741-4326/ac715e.

[18] E. Speth et al. "Overview of the RF source development programme at IPP Garching". In: *Nuclear Fusion* 46.6 (May 2006), S220. DOI: 10.1088/0029-5515/46/6/S03. URL: https://dx.doi.org/10.1088/0029-5515/46/6/S03.

[19] V Toigo et al. "The PRIMA Test Facility: SPIDER and MITICA test-beds for ITER neutral beam injectors". In: *New Journal of Physics* 19.8 (Aug. 2017), p. 085004. DOI: 10.1088/1367-2630/aa78e8. URL: https://dx.doi.org/10.1088/1367-2630/aa78e8.

[20] Roman Zagórski, Emanuele Sartori, and Gianluigi Serianni. "2-D Fluid Model for Discharge Analysis of the RF-Driven Prototype Ion Source for ITER NBI (SPIDER)". In: *IEEE Transactions on Plasma Science* (2022), pp. 1–7. ISSN: 1939-9375. DOI: 10.1109/TPS.2022.3175527.